Lian-Ping Wang[1]
Department of Mechanical Engineering,
University of Delaware,
Newark, DE 19716-3140
e-mail: lwang@udel.edu

Cheng Peng
Department of Mechanical Engineering,
University of Delaware,
Newark, DE 19716-3140
e-mail: cpengxpp@udel.edu

Zhaoli Guo
National Laboratory of Coal Combustion,
Huazhong University of Science and
Technology,
Wuhan 430074, China
e-mail: zlguo@hust.edu.cn

Zhaosheng Yu
Department of Mechanics,
Zhejiang University,
Hangzhou 310027, China
e-mail: yuzhaosheng@zju.edu.cn

Flow Modulation by Finite-Size Neutrally Buoyant Particles in a Turbulent Channel Flow

A fully mesoscopic, multiple-relaxation-time (MRT) lattice Boltzmann method (LBM) is developed to perform particle-resolved direct numerical simulation (DNS) of wall-bounded turbulent particle-laden flows. The fluid–solid particle interfaces are treated as sharp interfaces with no-slip and no-penetration conditions. The force and torque acting on a solid particle are computed by a local Galilean-invariant momentum exchange method. The first objective of the paper is to demonstrate that the approach yields accurate results for both single-phase and particle-laden turbulent channel flows, by comparing the LBM results to the published benchmark results and a full-macroscopic finite-difference direct-forcing (FDDF) approach. The second objective is to study turbulence modulations by finite-size solid particles in a turbulent channel flow and to demonstrate the effects of particle size. Neutrally buoyant particles with diameters 10% and 5% the channel width and a volume fraction of about 7% are considered. We found that the mean flow speed was reduced due to the presence of the solid particles, but the local phase-averaged flow dissipation was increased. The effects of finite particle size are reflected in the level and location of flow modulation, as well as in the volume fraction distribution and particle slip velocity near the wall. [DOI: 10.1115/1.4031691]

1 Introduction

Turbulent flows laden with solid particles or liquid droplets occur frequently in engineering, biological, and environmental applications. Examples include pneumatic conveying, pulverized coal combustion, spray drying and cooling, particulate pollution control, and fluid catalytic cracking, etc., see Refs. [1,2]. A turbulent particle-laden flow system is more complicated than its single-phase counterpart owing to a wider range of length and time scales and the additional parameters associated with the dispersed phase [3]. For a turbulent flow laden with nondeforming spherical particles, the length scales range from the particle diameter (d_p) and flow Kolmogorov length (η) to the integral length scale (L). When d_p/η is small and the volume fraction (ϕ_V) of the dispersed phase is low, the response of a particle to the local flow can be well described by an equation of motion [4], making it unnecessary to resolve the disturbance flow on the scale of the particle size. Most theoretical understanding for turbulent particle-laden flows has been developed based on these assumptions. Computationally, the condition of $d_p/\eta < 1$ partially justifies the use of point-particle based simulation (PPS) [5]. In the last 25 years, PPS has enabled researchers to discover and quantify a number of important phenomena in turbulent particle-laden flows including preferential concentration [6,7], turbulence modulation by inertial particles [8,9], particle deposition rate, and turbulent collision rate of inertial particles [5,10–13].

In many applications with high rate of flow dissipation, the particle size is comparable to or larger than the flow Kolmogorov length [14], which introduces finite-size effects greatly complicating the description of the flow system. Currently, the only rigorous method is to numerically resolve the disturbance flows around particles, known as the particle-resolved or interface-resolved simulation (PRS). This requires an explicit consideration of the no-slip boundary condition on the surface of each moving particle.

PRS of turbulent particle-laden flows involves direct simulation of the turbulent carrier flow and explicit and accurate treatment of many moving fluid–solid interfaces, such that all scales from turbulence integral scale to dissipation scales and particle size are directly resolved with scale separations determined by applications. In recent years, several PRS methods based on the Navier–Stokes (N–S) equations have been developed, with the particle–fluid interfaces treated by the immersed boundary method [15,16], direct-forcing [17,18], local analytical treatment [19], overset grid [14], force-coupling [20], or penalization method [21]. As reviewed in Refs. [22,23], these studies have contributed to the understanding of flow modulation by the inertial particles and the dynamic effects due to finite particle size.

As an alternative approach, the LBM has also been applied as a PRS method for turbulent particle-laden flows [22–26]. The LBM approach features a high-level data locality essential to efficient parallel implementation of PRS. Another advantage is that LBM has the flexibility and simplicity (i.e., via local bounce-back) for implementing fluid–solid and fluid–fluid interfacial boundary conditions. This offers the potential for the method to be applied to treat turbulent flows laden with nonspherical and deformable particles.

The main objective of this paper is to develop and test a fully mesoscopic LBM approach for simulating wall-bounded turbulent particle-laden flows. By fully mesoscopic, we mean that the bulk flow simulations, no-slip and no-penetration boundary conditions on the moving particle surfaces, and the computation of hydrodynamic force and torque acting on a moving particle is treated at the level of distribution function in LBM. It is crucial that the results can be compared directly to other approaches under the identical physical conditions. Previously, we have applied LBM to homogeneous isotropic particle-laden turbulent flows [22,23]. In a wall-bounded flow, the flow scales near the wall and away from the wall could be quite different, and to the best of our knowledge, there has not been a successful simulation of a particle-laden turbulent channel flow using LBM. There are, however, some first attempts to develop particle-resolved simulations of wall-bounded particle-laden flows using pseudospectral and finite-difference methods, with the moving particles treated by the immersed boundary method [16,27,28] or direct-forcing method [17].

From experimental perspective, particle-laden wall-bounded flows have played an important role in understanding turbulence modulation by solid particles. Previous experimental studies

[1]Corresponding author.

Contributed by the Fluids Engineering Division of ASME for publication in the Journal of Fluids Engineering. Manuscript received January 11, 2015; final manuscript received August 22, 2015; published online December 8, 2015. Assoc. Editor: E. E. Michaelides.

included particle-laden open channel flow [29], turbulent boundary layer [30,31], and turbulent pipe flow [32,33]. It is well known that the presence of small solid particles typically decreases the turbulence intensity due to enhanced viscous dissipation, whereas large particles can enhance the turbulence intensity due to undamped disturbances and wake effects [34,35]. Solid particle had also been observed to alter the critical Reynolds number for laminar to turbulent flow transition, where small particles delay transition to larger flow Reynolds numbers, and large particles cause transition at smaller Reynolds numbers [36]. In general, the nature and level of modulation depend on many factors including scales and geometric configurations of the carrier phase flow and particle characteristics, such as size, density, mass loading, particle distribution, and gravity. Finite-size particles may introduce both local viscous dissipation and kinetic energy production. Experimental studies mainly provide bulk flow statistics, however, they could not reveal detailed interactions between particles and turbulence at the scale of particle size. It is hoped that particle-resolved DNSs can provide a deep understanding of turbulence modulation by solid particles and effects of finite particle size on the dynamics of solid particles.

Specifically, we will validate our LBM approach by comparing LBM results to the published benchmark data for single-phase turbulent channel flow, and, for particle-laden turbulent channel flow, to results from a fully macroscopic FDDF approach [17,37]. Due to the complex nature of particle-laden turbulent flows and lack of experimental data at the identical conditions and at the microscale, the systematic intercomparisons between two completely different (mesoscopic versus macroscopic) computational approaches are much desired, in order to identify potential pitfalls in a given approach and inaccuracies in the simulation results. Another objective is to study turbulence modulations by finite-size solid particles in a turbulent channel flow and to demonstrate the effects of particle size. Following the study of Shao et al. [17], neutrally buoyant particles with diameters 10% and 5% the channel width and a volume fraction of about 7% are considered in this study.

The paper is organized as follows: In Sec. 2, the physical problem and the two computation approaches (LBM and FDDF) are described, along with important implementation details that lead to successful simulations of the particle-laden turbulent channel flow. The results are presented in Sec. 3, where we first discuss results from simulations of single-phase turbulent channel flow, by comparing our results with published benchmark data. We then analyze in some detail several aspects of turbulence modulations and particle distribution, to illustrate the effects of finite particle size. The summary and main conclusions are presented in Sec. 4.

2 Problem Statement and the Particle-Resolved DNS Approach

We consider a turbulent channel flow laden with finite-size solid particles, as sketched in Fig. 1(*a*), with x, y, and z representing the streamwise, transverse, and spanwise directions, respectively. The width of the channel is $2H$, and the domain size in the streamwise direction is L_x and in the spanwise is L_z. The turbulent flow is driven by a constant body force (or equivalently mean pressure gradient) in the x-direction. Periodic boundary condition is assumed in the x- and z-directions, and the no-slip condition on the two channel walls.

For the single-phase turbulent channel flow (i.e., without solid particles), the flow is mainly governed by the flow Reynolds number $\mathrm{Re} = \overline{U}H/\nu$, where ν is the kinematic viscosity and $\overline{U}$ is the mean flow speed. At the fully developed stage, force balance $2\tau_w L_x L_z = \rho g 2HL_x L_z$ leads to the expressions for the wall viscous shear stress τ_w and frictional velocity u^* as

$$\tau_w = \rho g H, \quad u^* = \sqrt{\frac{\tau_w}{\rho}} = \sqrt{Hg} \tag{1}$$

where ρ is the fluid density and g is the body force per unit mass. The frictional Reynolds number is $\mathrm{Re}_\tau = u^* H/\nu = H/(\nu/u^*)$, where ν/u^* is the length unit in the viscous sublayer. The large-scale eddy-turnover time is defined as H/u^*.

In this paper, we only consider neutral solid particles of density $\rho_p = \rho$. To keep the flow driving force for the particle–fluid system the same, the same body force g is applied in the x-direction inside the solid particles. The only difference from the single-phase flow is then the presence of the moving fluid–solid interfaces where the no-slip condition is to be satisfied. There are two new governing parameters in the particle-laden flow. The first is the particle size relative to the half channel width a_p/H, where a_p is the radius of a solid particle. The second is the volume fraction of the particulate phase, $\phi_V = \frac{4n\pi a_p^3/3}{2HL_xL_z}$, where n is the particle number density.

2.1 The LBM. Advances in computer resources, numerical methods, and algorithms have made it possible, in the past decade, to conduct interface-resolved simulations of a turbulent particle-laden flow. Conventional computational fluid dynamics (CFD) makes use of the macroscopic N–S equations. In this study, the turbulent channel flow with many moving solid–fluid interfaces is solved by a mesoscopic computational approach known as the LBM. The LBM approach is based on a kinetic formulation and could have certain advantages over the conventional N–S based CFD [38,39]. The basic idea of LBM is to design an optimal kinetic model based on the Boltzmann equation that would produce the essentially exact N–S equations. There are two drawbacks of LBM, when compared with N–S based CFD: LBM solves a larger number of variables (typically 15 or 19 particle distributions at a given lattice point in three-dimensional); due to its short history, the general fluid mechanics community is less familiar with its capability, accuracy, and reliability and related implementation issues for the type of complex flows we intend to address here. These drawbacks, however, are outweighed by its tremendous computational advantages including: (1) quasi-linear nature of the lattice Boltzmann equation, (2) ease of imposing no-

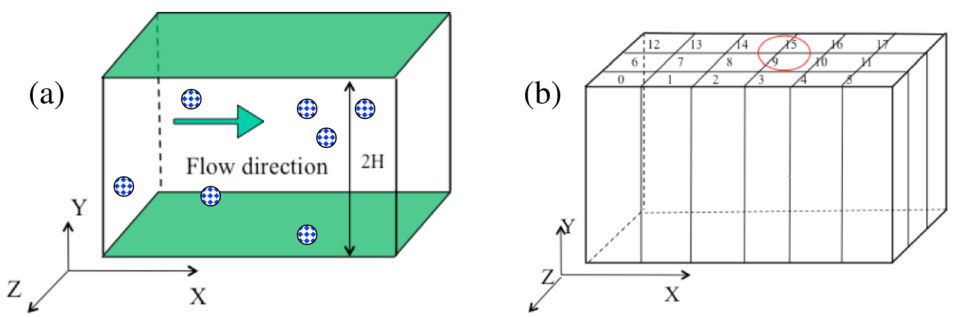

Fig. 1 Sketches of (*a*) the coordinate system used for the channel flow simulation and (*b*) the two-dimensional domain decomposition for message passing interface parallel implementation

slip boundary conditions on solid walls in complex geometry, (3) straightforward coding and parallelization, and (4) flexibilities in incorporating interfacial physics in multiphase flows. Specifically, the accuracy and reliability of LBM as a DNS tool have been documented in many studies, e.g., Refs. [22,23,40,41]. For single-phase turbulence, the use of double spatial resolution allows LBM to produce results as accurate as the pseudospectral method based on the N–S equations [22,23,40]. Due to its inherent low numerical dissipation (by using the exact streaming–collision mechanics), mesoscopic conservation laws, and better rotational invariant property or better symmetry in comparison with the N–S solvers, LBM of nominal second-order accuracy in space and time is likely to perform better than a second-order finite-difference or finite-volume scheme based on the N–S equations [40]. The accuracy of LBM in simulating particle-laden turbulent flow is a topic relevant to the current study. The key here is to resolve the boundary layer on the solid particle surface due to the relative motion of the fluid. In this work, the advantages of LBM are mainly reflected in treating the moving boundaries at the fluid–solid interfaces [42].

In this paper, we wish to develop a numerical method to solve the turbulent particle-laden channel flow stated above, with local flow around each particle resolved. Following our recent studies [22,23], the MRT LBM [43] is applied for this particle-resolved turbulent flow simulation. Since a thorough discussion of the method including a few validation case has already been presented in Refs. [22,23], here we only summarize the essential components of the method, along with the latest improvements.

The MRT LBM solves the evolution of mesoscopic particle distribution function by a lattice Boltzmann equation

$$\mathbf{f}(\mathbf{x}+\mathbf{e}_\alpha\delta t, t+\delta t) = \mathbf{f}(\mathbf{x},t) - \mathbf{M}^{-1}\cdot\mathbf{S}\cdot[\mathbf{m}-\mathbf{m}^{(\mathrm{eq})}] + \mathbf{Q} \tag{2}$$

where $\mathbf{f}$ is a 19-component vector distribution function representing the probability of a lattice fluid particle taking a specific discrete velocity, $\mathbf{e}_\alpha$ ($\alpha = 0, 1, 2,., 18$) are the 19 discrete microscopic velocities (to be defined below for the D3Q19 model), δt is the lattice time step, and $\mathbf{M}$ is an orthogonal transformation matrix converting the vector distribution function $\mathbf{f}$ from the discrete velocity space to the moments $\mathbf{m}$ (a vector of 19 components). The collision relaxations are applied over the components of $\mathbf{m}$. The term $\mathbf{Q}$ denotes a forcing field in the mesoscopic space to produce a desired nonuniform, time-dependent, large-scale physical space forcing field $\rho_0\mathbf{q}(\mathbf{x},t)$. Its implementation follows the MRT formulation [44,45] that is free of low-order discrete lattice errors, and the details were discussed in Ref. [23].

The basic idea of MRT is that the streaming substep is handled in the microscopic lattice-velocity space but the collision substep is performed in the moment space. The transformation between the microscopic velocity space and the moment space is carried out by matrix operations as $\mathbf{m} = \mathbf{M}\cdot\mathbf{f}$, $\mathbf{f} = \mathbf{M}^{-1}\cdot\mathbf{m}$. The diagonal relaxation matrix $\mathbf{S}$ specifies the relaxation rates for the non-conserved moments.

The macroscopic hydrodynamic variables, including density ρ, momentum, and pressure p, are obtained from the moments of the mesoscopic distribution function $\mathbf{f}$. In the nearly incompressible formulation, they are given as

$$\rho = \rho_0 + \delta\rho, \quad \rho_0 = 1 \tag{3}$$

$$\delta\rho = \sum_\alpha f_\alpha, \quad \rho_0\mathbf{u} = \sum_\alpha f_\alpha\mathbf{e}_\alpha + \frac{\delta t}{2}\rho_0\mathbf{q}(\mathbf{x},t), \quad p = \delta\rho c_s^2 \tag{4}$$

where $\mathbf{u}$ is the macroscopic fluid velocity, and the sound speed c_s is equal to $1/\sqrt{3}$ in lattice units. In our implementation, the distribution functions $\mathbf{f}$ are solved only at the fluid lattice nodes.

The design details of the MRT model include three parts. The first part is to choose a proper set of discrete microscopic velocities. The standard D3Q19 model is used here with the following 19 velocities: $\mathbf{e}_0 = (0,0,0)$, $\mathbf{e}_{1,2} = (\pm1,0,0)$, $\mathbf{e}_{3,4} = (0,\pm1,0)$, $\mathbf{e}_{5,6} = (0,0,\pm1)$, $\mathbf{e}_{7,8,9,10} = (\pm1,\pm1,0)$, $\mathbf{e}_{11,12,13,14} = (\pm1,0,\pm1)$, and $\mathbf{e}_{15,16,17,18} = (0,\pm1,\pm1)$. The use of only 15 or 19 lattice velocities in three-dimensional LBM simulations is adequate for incompressible flows. This can be proven rigorously by the Gauss–Hermite quadrature of the moment integrations [46]. If compressible flows or moment equations at higher-orders (beyond the N–S) are considered, then more lattice velocities will be needed [47]. At the level of incompressible N–S flow, increasing discrete velocities may give better results, but it can be expected that the results are similar, since they all converge to the nearly incompressible N–S equations in terms of the Chapman–Enskog analysis.

The second part is to specify the 19 orthogonal moments: $\mathbf{m} = (\tilde{\rho}, e, \varepsilon, j_x, q_x, j_y, q_y, j_z, q_z, 3p_{xx}, 3\pi_{xx}, p_{ww}, \pi_{ww}, p_{xy}, p_{yz}, p_{xz}, m_x, m_y, m_z)^{\mathrm{T}}$. These are defined through the elements of the transformation matrix (each subscript runs from 0 to 18) as

$$\begin{aligned}
&M_{0,\alpha} = ||\mathbf{e}_\alpha||^0, \quad M_{1,\alpha} = 19||\mathbf{e}_\alpha||^2 - 30\\
&M_{2,\alpha} = (21||\mathbf{e}_\alpha||^4 - 53||\mathbf{e}_\alpha||^2 + 24)/2\\
&M_{3,\alpha} = e_{\alpha x}, \quad M_{5,\alpha} = e_{\alpha y}, \quad M_{7,\alpha} = e_{\alpha z}\\
&M_{4,\alpha} = (5||\mathbf{e}_\alpha||^2 - 9)e_{\alpha x}, \quad M_{6,\alpha} = (5||\mathbf{e}_\alpha||^2 - 9)e_{\alpha y}\\
&M_{8,\alpha} = (5||\mathbf{e}_\alpha||^2 - 9)e_{\alpha z}\\
&M_{9,\alpha} = 3e_{\alpha x}^2 - ||\mathbf{e}_\alpha||^2, \quad M_{11,\alpha} = e_{\alpha y}^2 - e_{\alpha z}^2\\
&M_{13,\alpha} = e_{\alpha x}e_{\alpha y}, \quad M_{14,\alpha} = e_{\alpha y}e_{\alpha z}, \quad M_{15,\alpha} = e_{\alpha x}e_{\alpha z}\\
&M_{10,\alpha} = (3||\mathbf{e}_\alpha||^2 - 5)(3e_{\alpha x}^2 - ||\mathbf{e}_\alpha||^2)\\
&M_{12,\alpha} = (3||\mathbf{e}_\alpha||^2 - 5)(e_{\alpha y}^2 - e_{\alpha z}^2)\\
&M_{16,\alpha} = (e_{\alpha y}^2 - e_{\alpha z}^2)e_{\alpha x}, \quad M_{17,\alpha} = (e_{\alpha z}^2 - e_{\alpha x}^2)e_{\alpha y}\\
&M_{18,\alpha} = (e_{\alpha x}^2 - e_{\alpha y}^2)e_{\alpha z}
\end{aligned} \tag{5}$$

Then, the Chapman–Enskog multiscaling analysis can be performed on Eq. (2), to formulate the equilibrium moments such that the Euler and N–S equations would be satisfied at the first and second-order, respectively. This will lead to the following results for $\mathbf{m}^{(\mathrm{eq})}$ with a few adjustable parameters:

$$\begin{aligned}
&\tilde{\rho}^{(\mathrm{eq})} = \tilde{\rho} = \delta\rho, \quad e^{(\mathrm{eq})} = -11\delta\rho + \frac{19}{\rho_0}\left(j_x^2 + j_y^2 + j_z^2\right)\\
&\varepsilon^{(\mathrm{eq})} = \omega_\varepsilon\delta\rho + \frac{\omega_{\varepsilon j}}{\rho_0}\left(j_x^2 + j_y^2 + j_z^2\right)\\
&j_x^{(\mathrm{eq})} = j_x = \rho_0 u_x, \quad j_y^{(\mathrm{eq})} = j_y = \rho_0 u_y, \quad j_z^{(\mathrm{eq})} = j_z = \rho_0 u_z\\
&q_x^{(\mathrm{eq})} = -\frac{2}{3}j_x, \quad q_y^{(\mathrm{eq})} = -\frac{2}{3}j_y, \quad q_z^{(\mathrm{eq})} = -\frac{2}{3}j_z\\
&p_{xx}^{(\mathrm{eq})} = \frac{1}{3\rho_0}\left[2j_x^2 - \left(j_y^2 + j_z^2\right)\right], \quad p_{ww}^{(\mathrm{eq})} = \frac{1}{\rho_0}\left[j_y^2 - j_z^2\right]\\
&p_{xy}^{(\mathrm{eq})} = \frac{1}{\rho_0}j_x j_y, \quad p_{yz}^{(\mathrm{eq})} = \frac{1}{\rho_0}j_y j_z, \quad p_{xz}^{(\mathrm{eq})} = \frac{1}{\rho_0}j_x j_z\\
&\pi_{xx}^{(\mathrm{eq})} = \omega_{xx}p_{xx}^{(\mathrm{eq})}, \quad \pi_{ww}^{(\mathrm{eq})} = \omega_{xx}p_{ww}^{(\mathrm{eq})}\\
&m_x^{(\mathrm{eq})} = m_y^{(\mathrm{eq})} = m_z^{(\mathrm{eq})} = 0
\end{aligned} \tag{6}$$

Finally, the relaxation of unconserved moments is described as $\mathbf{S} = \mathrm{diag}(0, s_1, s_2, 0, s_4, 0, s_4, 0, s_4, s_9, s_{10}, s_9, s_{10}, s_{13}, s_{13}, s_{13}, s_{16}, s_{16}, s_{16})$. The kinematic viscosity ν of the model is given as $\nu = (s_9^{-1} - 1)c_s^2\delta t$.

In this study, the specific model parameters are taken from Ref. [43] with some modification to s_1 and s_{16}, and they are $\omega_\varepsilon = 0.0$, $\omega_{\varepsilon j} = -475/63$, $\omega_{xx} = 0.0$, $s_1 = 1.5$, $s_2 = 1.4$, $s_4 = 1.2$, $s_9 = \delta t/(3\nu + 0.5\delta t)$, $s_{10} = 1.4$, $s_{13} = s_9$, and $s_{16} = 1.98$. The above completes the description of the D3Q19 MRT LBM model.

2.2 Accurate Treatment of Moving Fluid–Solid Interfaces in the LBM Approach. When moving solid particles are present, additional implementation details need to be considered. The

no-slip condition at the moving fluid–solid interfaces is treated by a quadratic interpolated bounce-back scheme [48]. In this scheme, the exact location where a lattice link and the solid particle boundary intersect is considered; therefore, the curved solid–fluid interface is explicitly represented. The quadratic interpolation also maintains the second-order accuracy of the LBM approach [42]. When a solid particle moves, a solid lattice node may become a fluid node with unknown distribution functions. The missing distribution functions for the new fluid lattice node are constructed by a newly developed velocity-constrained extrapolation method [42]. The basic idea is to first estimate the missing distribution functions using the three-point normal extrapolation refilling proposed in Ref. [48]. Then, a refinement step is performed to constrain the velocity at the new fluid lattice node to the local solid velocity. This is conveniently carried out within the MRT formulation by transforming the distributions into the moment space, correcting for the momentum, and updating the distributions through an inverse transformation. We find that this constraint can significantly reduce the fluctuations in the hydrodynamic forces when compared to the unconstrained normal extrapolation [42]. Even more importantly, before introducing this constrained scheme, we used equilibrium plus nonequilibrium refilling [49] and encountered numerical instability that causes the code to diverge. After replaced by the velocity-constrained normal extrapolation refilling, our particle-laden turbulent channel flow code has a much better numerical stability.

Care has to be taken to ensure periodic boundary conditions associated with finite-size solid particles. A solid particle is defined by its center, radius, translational, and angular velocity, these are saved in all processors. Essentially, a subdomain near the physical domain boundary will have part of its neighboring domain composed of the periodic image of the physical domain. This is processed by assign a unique ID to each subdomain, as well as IDs for all its neighboring subdomains.

The hydrodynamic force $\mathbf{F}_i$ and torque $\mathbf{T}_i$ acting on the ith particle are calculated during the interpolated bounce-back procedure by the recently developed Galilean-invariant momentum exchange method [42,50]. In this method, when lattice fluid particles interact with a solid particle boundary, the loss of fluid momentum *relative to the local solid surface* is summed over all lattice links crossing the boundary of a solid particle. This net loss is interpreted as the hydrodynamic force acting on the solid particle. Namely, the lattice particle velocity relative to the local solid boundary velocity is used to compute the force and torque acting on a solid particle. It is very important that we enforce this local Galilean invariance property in order to produce physically correct results, as discussed in Ref. [42]. The particle translational velocity, position, angular velocity, and displacement are then updated as

$$\mathbf{V}_i^{t+\delta t} = \mathbf{V}_i^t + \frac{1}{M_p}\left(\frac{\mathbf{F}_i^{t+\delta t/2} + \mathbf{F}_i^{t-\delta t/2}}{2} + \sum_j \mathbf{F}_{ij}^t\right)\delta t \tag{7}$$

$$\mathbf{Y}_i^{t+\delta t} = \mathbf{Y}_i^t + \frac{1}{2}\left(\mathbf{V}_i^t + \mathbf{V}_i^{t+\delta t}\right)\delta t \tag{8}$$

$$\Omega_i^{t+\delta t} = \Omega_i^t + \frac{1}{I_p}\left(\frac{\mathbf{T}_i^{t+\delta t/2} + \mathbf{T}_i^{t-\delta t/2}}{2}\right)\delta t \tag{9}$$

$$\Theta_i^{t+\delta t} = \Theta_i^t + \frac{1}{2}\left(\Omega_i^t + \Omega_i^{t+\delta t}\right)\delta t \tag{10}$$

where M_p and $I_p \equiv 2/5 M_p a_{p,i}^2$ are the mass and moment of inertia of the ith particle, R_i is the particle radius, and $\mathbf{F}_{ij}$ represents the unresolved interaction force acting on the ith particle due to its interaction with jth particle (e.g., the lubrication force correction, see Refs. [51,52]). In this study, a simple pairwise repulsive force model, same as what was used in Refs. [22,53], is applied to prevent particles from overlapping, when the gap distance is below 2 lattice units. A similar model is used to model near-field particle–channel wall interactions. Since the volume fraction is finite, this artificial lubrication model may have an effect on the results—an aspect that should be studied in the future.

In order to assess the relative changes of the flow statistics, a single-phase turbulent channel flow was simulated first as a reference flow to analyze the results of a particle-laden turbulent channel flow. In a typical single-phase channel flow simulation, we initialize the flow field using a prescribed mean flow that is consistent with the profile for the linear viscous sublayer and the inertial sublayer. To speed up the transition from the initial flow to the fully developed turbulent channel flow, we added a strong nonuniform, divergence-free forcing field to the flow for a short period of time [54]. Immediately after the nonlinear flow instability was excited, we switched off this nonuniform forcing, leaving only the constant body force g to drive the turbulent flow.

On the other hand, in the simulation of a particle-laden flow, the disturbances due to the solid particles provide a natural mechanism to excite the flow instability that will lead to a turbulent flow. Therefore, no extra forcing was applied.

The MRT LBM code was parallelized using two-dimensional domain decomposition where the domain is divided in x- and z-directions as shown in Fig. 1(*b*). Since the data communications are with the neighboring subdomains only, a nearly ideal scalability was realized.

2.3 The FDDF Approach. A major objective of this paper is to compare our LBM results (a mesoscopic approach) to results from an FDDF method (a macroscopic continuum-based approach). Here, we briefly describe the key elements of the FDDF approach.

The FDDF method employed belongs to a family of fictitious domain methods. The key idea is to fill the domains inside the solid particles with the same fluid as the surroundings and the Lagrange multiplier (i.e., a pseudobody force) is introduced into the momentum equation to enforce the interior (fictitious) fluid to satisfy the constraint of rigid-body motion [53]. A fractional-step time integration scheme is used to decouple the system into the fluid-flow subproblem and the particle-motion subproblem. The fluid-flow subproblem is solved with a second-order accurate finite-difference method and a projection method on a uniform half-staggered grid. The particle-motion subproblem is solved with the direct-forcing scheme. The trilinear function is used to interpolate the fluid velocity from the Eulerian nodes to the Lagrangian marker locations and to distribute the pseudobody force from the Lagrangian marker locations to the Eulerian nodes. The reader is referred to Yu and Shao [37] for the details of the FDDF method. The method has been applied to the simulations of the particle-laden turbulent channel [17] and pipe flows [55] at a given flow flux and the transitional pipe flow [56].

3 Results

In this section, we present results on both single-phase and particle-laden turbulent channel flows. We focus our discussions on two general questions. The first is how the statistics of a particle-laden turbulent channel flow differ from those of single-phase turbulent channel flow and how this difference depends on the size of the particles under a given particle volume fraction. The second question is how reliable our simulation results are for simulations of such complex multiphase turbulent flows.

3.1 Single-Phase Turbulent Channel Flow. The single-phase turbulent channel flow represents one of the simplest wall-bounded turbulent flows as the flow is homogeneous in both streamwise and spanwise directions. We are interested in flow statistics when the flow becomes stationary, namely, the rate of work done by the driving body force is balanced by the net viscous

Table 1 Parameter settings in the simulations of single-phase turbulent channel flow

Run	$L_x \times L_y \times L_z$	$N_x \times N_y \times N_z$	Re_τ	$\delta y/(\nu/u^*)$ (<2.25 [41])
LBM–SP	$4.020H \times 2H \times 2.010H$	$400 \times 199 \times 200$	180	1.806
YuL4–SP	$4H \times 2H \times 2H$	$256 \times 128 \times 128$	180	2.81
YuL8–SP	$8H \times 2H \times 4H$	$512 \times 128 \times 256$	180	2.81
Stanford	$4\pi H \times 2H \times 4\pi H/3$	$128 \times 128 \times 128$	178.1	$0.054 \rightarrow 4.4$

dissipation in the flow. The parameter setting of the single-phase turbulent channel flow in our LBM simulation and two FDDF simulations is shown in Table 1, along with a pseudospectral simulation (denoted by "Stanford") done by the Stanford group [57,58]. In the spectral (SP) simulation, the flow is expanded in terms of Fourier series in the x-and z-directions and Chebyshev polynomials in the transverse direction. The friction Reynolds numbers are comparable in these simulations. In this preliminary study, we consider primarily a computational domain size of $4H \times 2H \times 2H$ (LBM–SP and YuL4–SP). A larger domain ($8H \times 2H \times 4H$) was also used in the FDDF simulation (YuL8–SP) to gain some understanding of the effect of domain size on the turbulence statistics. In both LBM and FDDF simulations, a uniform grid was used. The spectral simulation used a much larger domain size ($4\pi H \times 2H \times 4\pi H/3$) and a nonuniform grid in the transverse direction which allows the linear viscous sublayer to be adequately resolved.

The viscosity in the LBM–SP simulation was set to 0.0036, above the limiting value of 0.00254 [43] below which the MRT model may become unstable. The friction velocity was set to 0.006513, which resulted in a maximum local velocity magnitude of about 0.14 or a maximum local Mach number (defined as the maximum local velocity magnitude over the speed of sound c_s) of about 0.24; thus, the compressibility effect can be neglected. Note that the grid resolution is checked by the value of $\delta y u^*/\nu$, where δy is the grid spacing. Based on the simulations of a turbulent channel flow using the Bhatnagar–Gross–Krook (BGK) LBM model, Lammers et al. [41] suggested that this value should be kept less than 2.25 for a well-resolved simulation. If this same criterion is applied to the FDDF simulations, they were perhaps somewhat under-resolved.

Applying the Reynolds decomposition and noting that the flow is homogeneous in x- and z-directions, we can write $u_x = U(y) + u'_x(x,y,z)$, $u_y = u'_y(x,y,z)$, $u_z = u'_z(x,y,z)$, $p = P(y) + p'(x,y,z)$, where $U(y)$ and $P(y)$ are the mean flow velocity and pressure, respectively. When the flow reaches the stationary stage, the x-momentum balance equation is

$$0 = \frac{d\langle -u'_x u'_y \rangle}{dy} + g + \nu \frac{d^2 U}{dy^2} \tag{11}$$

which leads to the total shear stress (Reynolds plus viscous) distribution as

$$\frac{1}{u^{*2}}\left[\langle -u'_x u'_y \rangle + \nu \frac{U}{dy}\right] = -\frac{y_c}{H} \tag{12}$$

where y_c is the distance relative to the channel center, and y is the distance from a wall. Figure 2 compares the simulated Reynolds shear stress profiles in half of the channel. The channel center is at $y/(2H) = 0.5$. Although our domain size is smaller than the domain size in the spectral simulation, the results are in excellent agreement with the spectral simulation results. The two FDDF results show a slightly smaller peak Reynolds stress, which could be due to the inadequate grid resolution used (Table 1).

Next, the mean velocity profiles are compared on a log–linear plot in Fig. 3. In the wall length unit, the channel center is at $y^+ = 180$. Once again, the LBM–SP result is in excellent agreement with the spectral simulation result for most of the locations, except in the channel center region where the LBM–SP result is

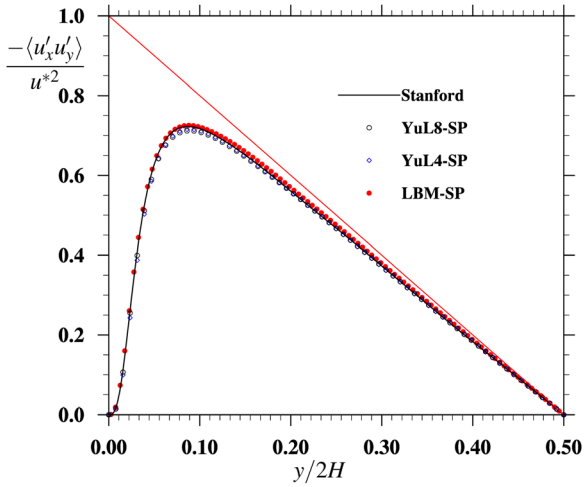

Fig. 2 Turbulent Reynolds shear stress profiles in half of the channel. All quantities are normalized by u^{*2}. The thin diagonal line denotes the total shear stress, so the difference between this straight line and the data represents the viscous shear stress due to the mean flow.

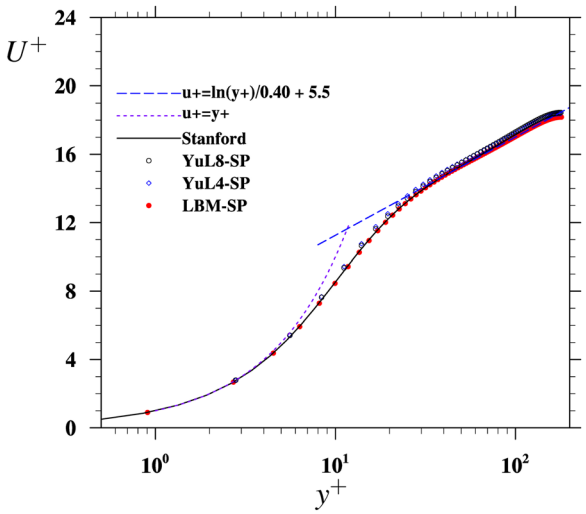

Fig. 3 Comparison of the mean flow velocity profiles of the simulated single-phase turbulent channel flows

about 0.7% less than the spectral result. The profile fits well the standard linear viscous sublayer scaling for $y^+ < 5$, and the inertial sublayer scaling starting at $y^+ > 30$. The FDDF results appear to slightly overpredict the mean velocity for $y^+ > 5$ with both domain sizes. The average flow speeds in LBM–SP, Yu4L-SP, Yu8L-SP, and Stanford are 15.65, 15.84, 15.85, and 15.69, respectively. Note that the spectral simulation used a nonuniform grid, so a cubic spine interpolation is first used to obtain the velocity at the same uniform y^+ locations as in Yu4L-SP before the average flow speed is processed.

The root-mean-squared (RMS) velocity profiles are shown in Fig. 4. Here, $u^+_{\mathrm{RMS}} \equiv \sqrt{\langle u'^2_x \rangle}/u^*$, $v^+_{\mathrm{RMS}} \equiv \sqrt{\langle u'^2_y \rangle}/u^*$, and

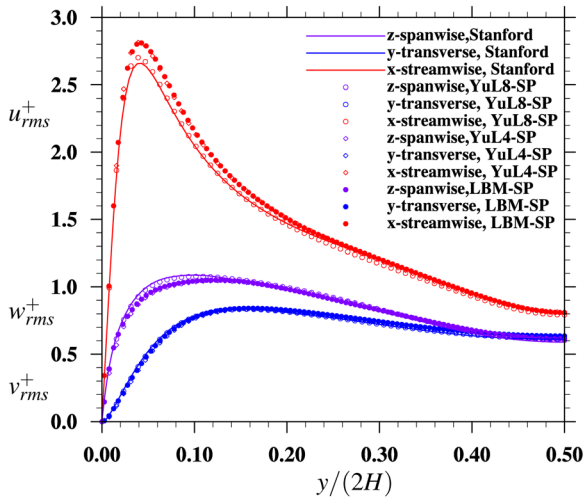

Fig. 4 Comparison of the RMS velocity profiles of the simulated single-phase turbulent channel flows

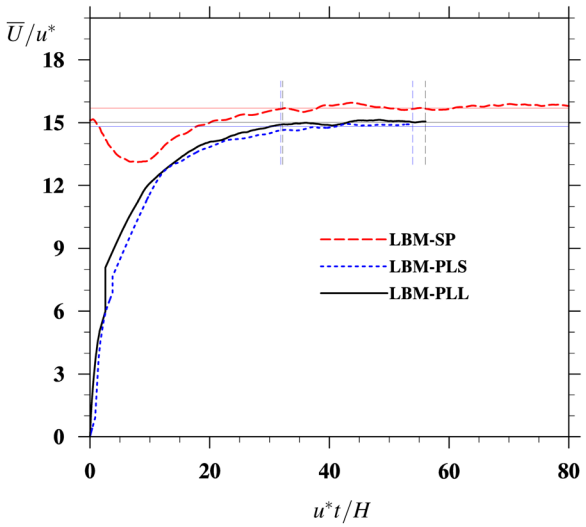

Fig. 5 The time evolution of mean flow speed (averaged over *y*) in the LBM simulations. The two vertical dash lines indicate the stationary stage ($32.2 < t^* < 56.1$) used to obtain average statistics for LBM–PLL. The two blue vertical lines indicate the stationary stage ($31.9 < t^* < 53.9$) used to obtain average statistics for LBM–PLS. The three horizontal lines mark 15.74, 15.02, and 14.82, respectively.

$w^+_{\mathrm{RMS}} \equiv \sqrt{\langle u_z'^2 \rangle}/u^*$. Overall, the profiles from different approaches are in reasonable agreement. Specifically, the LBM–SP results are in excellent agreement with the YuL4–SP results, for all three components, although there are some discrepancy in the average velocity profiles (see Fig. 3). These two simulations used the same small domain ($4H \times 2H \times 2H$); as a result, the streamwise RMS velocities are larger than the spectral result (about 6.5% larger at the peak location $y+ = 15.4$), and the spanwise RMS velocities are less than the spectral result (4.3% smaller at the peak location $y+ = 35.1$). Here, the peak locations are chosen as per the respective spectral result. These discrepancies are attributed to the use of different domain sizes since the YuL8–SP results are in much better agreement with the spectral results. The transverse RMS velocity profile appears to be almost independent of the domain size.

In summary, the comparisons of the LBM–SP results to the FDDF results and the spectral results show that the turbulence profiles are accurately simulated by the LBM approach. The LBM–SP simulation produces stress profile and mean velocity profile that are in excellent agreement with those from the spectral simulation. At the same domain size, the RMS velocity profiles of the LB-SP and YuL4–SP simulations are in excellent agreement. The domain size affects slightly the RMS velocities in the streamwise and spanwise directions, but has negligible effect on the RMS velocity in the transverse direction.

3.2 Particle-Laden Turbulent Channel Flow. The parameters for particle-laden simulations to be discussed are shown in Table 2. We consider here only neutrally buoyant solid particles ($\rho_p = \rho_f$) with a same body force pointing in the streamwise direction only. Under such a special case, there are only two governing parameters associated with the particulate phase, namely, the dimensionless particle radius (a_p/H) and the average particle volume fraction ϕ_V. Two particle sizes ($a_p/H = 0.10$ and $a_p/H = 0.05$) are considered and they are denoted as PPL (particle-laden flow with large-size solid particles) and PLS (particle-laden flow with small-size solid particles). The particle volume fraction ϕ_V was set to about 7% for all runs. Note that the resolution in the LBM runs is increased by 50% in each direction (Table 2) when compared to the single-phase LBM simulation (Table 1), to better resolve the disturbance flows due to solid particles and to overcome potential numerical stability. The kinematic viscosity for the LBM–PLL and LBM–PLS runs was set to 0.0040 and 0.0036, respectively; and friction velocity was reduced to 0.004816 and 0.004334, respectively.

3.2.1 Turbulence Modulation. In Fig. 5, we show the phase-averaged mean flow speed (averaged over y) as a function of non-dimensional time $t^* \equiv tu^*/H$. The mean flow speed can be expressed as

$$\overline{U} = \frac{1}{(1-\phi_V)L_y}\int_y [1-\Psi_p(y)]U(y)dy \tag{13}$$

where $U(y)$ is the phase-averaged fluid velocity at a given y location, and Ψ_p is the percentage of lattice nodes covered by solid particles at a given y. Clearly,

$$\phi_V = \frac{1}{L_y}\int_y \Psi_p(y)dy \tag{14}$$

In the LBM–SP run, the flow was initialized with a mean flow and an extra nonuniform force field [54] was applied to excite the turbulent flow for $0 < t^* < 3.24$. During this period of extra forcing, the mean flow speed decreases and kinetic energy is quickly transferred from the mean flow to the turbulent fluctuations. After $t^* = 3.24$, there is a further reduction in the mean flow speed

Table 2 Parameter settings in the simulations of particle-laden turbulent channel flow

Run	$L_x \times L_y \times L_z$	$L_x \times L_y \times L_z$	a_p	N_p	Re_τ	$\delta y/(\nu/u^*)$ (<2.25 [41])	a_p/H	ϕ_V (%)
LBM–PLL	$4.013H \times 2H \times 2.007H$	$600 \times 299 \times 300$	15.0	270	180	1.204	0.10033	7.09
LBM–PLS	$4.013H \times 2H \times 2.007H$	$600 \times 299 \times 300$	7.5	2160	180	1.204	0.05017	7.09
YuL4–PLL	$4H \times 2H \times 2H$	$256 \times 128 \times 128$	6.4	270	180	2.81	0.10	7.07
YuL4–PLS	$4H \times 2H \times 2H$	$256 \times 128 \times 128$	3.2	2160	180	2.81	0.05	7.07
YuL8–PLL	$8H \times 2H \times 4H$	$512 \times 128 \times 256$	6.4	1080	180	2.81	0.10	7.07

before the mean flow rebounds and gradually reaches to a stationary value of about $15.65u^*$ starting at $t^* \approx 30$. While for the particle-laden flow runs, the initial flow is static and an augmented constant body force (up to $10\rho_0 g$) was applied for $0 < t^* < 0.3$. The force was gradually reduced to the normal value ($\rho_0 g$) from $t^* = 0.3$ to $t^* = 1.5$. Note that there is a jump at a later time ($t^* \approx 3$ or $t^* \approx 5$)—this is due to a change in the friction velocity and viscosity in the simulations; initially, we used a larger u^* and later decided to reduced u^* for better numerical stability and accuracy. Interestingly, regardless of type of the flows and the method used to accelerate the flow development, the flows reach the stationary stage at $t^* \approx 30$. For the results to be presented below, the time intervals used to obtain the average flow statistics for LBM–SP, LBM–PLL, and LBM–PLS are $40.5 < t^* < 115.$, $32.2 < t^* < 56.1$, $31.9 < t^* < 53.9$, respectively.

At the stationary stage, all the LBM flows are driven by a same body force in the streamwise direction. Therefore, the net rate of work applied to the system is

$$\dot{\mathcal{P}} = \frac{\mathcal{V}g}{L_y}\int_y \left[(1-\Psi_p)\rho U(y) + \Psi_p(y)\rho_p U_p(y)\right]dy \tag{15}$$

$$= \mathcal{V}\rho g\left[(1-\phi_V)\overline{U} + \frac{\rho_p}{\rho}\phi_V\overline{U_p}\right] \tag{16}$$

$$= \rho\mathcal{V}\frac{u^{*2}}{H}\left[(1-\phi_V)\overline{U} + \frac{\rho_p}{\rho}\phi_V\overline{U_p}\right] \tag{17}$$

where $\mathcal{V} = L_x L_y L_z$ is the volume of the computational domain, U_p is the velocity averaged over all lattice nodes covered by solid particles (the local velocity within a solid particle is computed according to the solid body rotation), and $\overline{U_p}$ is the phase-averaged velocity over all lattice nodes covered by the solid particles

$$\overline{U}_p = \frac{1}{\phi_V L_y}\int_y \Psi_p(y)U_p(y)dy \tag{18}$$

This rate of work (or the rate of loss of potential energy of the system) is balanced by the net viscous dissipation within the fluid phase

$$\dot{\mathcal{D}} = \rho L_x L_z \int_y [1-\Psi_p(y)]\varepsilon_f(y)dy = \rho\mathcal{V}(1-\phi_V)\overline{\varepsilon_f} \tag{19}$$

where

$$\varepsilon_f(y) = 2\nu\langle s_{ij}(x,y,z)s_{ij}(x,y,z)\rangle \tag{20}$$

$$\overline{\varepsilon_f} = \frac{1}{(1-\phi_V)L_y}\int_y \left[1-\Psi_p(y)\right]\varepsilon_f(y)dy \tag{21}$$

with $\langle ...\rangle$ denotes average over the two homogeneous directions within the fluid phase and the local strain rate $s_{ij} \equiv (\partial u_i/\partial x_j + \partial u_j/\partial x_i)/2$.

Combining Eqs. (17) and (19), we obtain

$$\frac{\overline{\varepsilon_f}H}{u^{*3}} = \overline{U^+} + \frac{\phi_V}{1-\phi_V}\frac{\rho_p}{\rho}\overline{U_p^+} \tag{22}$$

Therefore, the phase-averaged dimensionless dissipation rate depends on the relative magnitudes of the phase-averaged mean speeds.

Figure 5 shows that the phase-averaged mean fluid speeds are $15.74u^*$, $15.02u^*$, and $14.82u^*$, respectively, for LBM–SP, LBM–PLL, and LBM–PLS. Namely, $\overline{U^+}$ is reduced by 4.57% and 5.84%, respectively, due to the presence of large solid particles and small solid particles, respectively.

The distributions of fluid-phase-averaged velocity U^+ are shown in Fig. 6 in both log–linear and linear–linear plots. In the linear viscous sublayer ($y^+ < 5$), the velocity profiles overlap and are close to the single-phase profile $U^+ = y^+$. This is understandable as the particle local volume percentage Ψ_p in this region is very small (1 % or less, see Fig. 13 below) so the effect in the particulate phase seems negligible. In the inertial sublayer, the velocity is reduced and the reduction is larger for the smaller particle size. The strongest modulations to the mean flow, relative to the single-phase flow, occur in the region ($10 < y^+ < 100$) between the wall and the channel centerline. The reductions are larger in the FDDF simulations when compared to the LBM simulations.

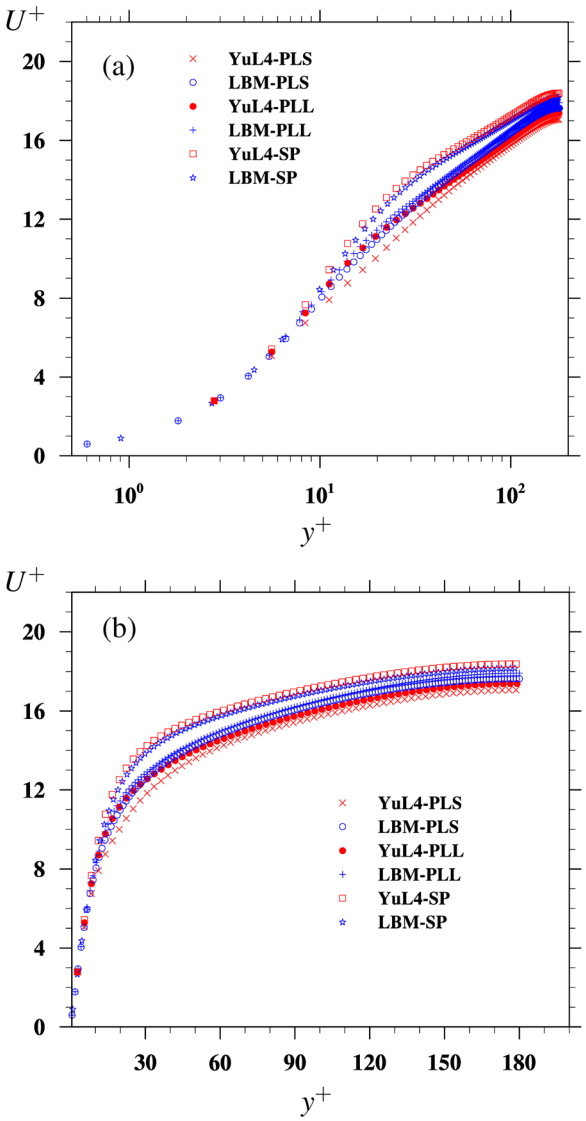

Fig. 6 The mean velocity profiles from both the LBM and FDDF simulations with a domain size of $4H\times2H\times2H$: (*a*) log–linear plot and (*b*) linear–linear plot

Pan and Banerjee [27] (hereafter PB97) developed an approximate particle-resolved simulation method and studied turbulence modulation in a particle-laden turbulent channel (with no-slip bottom wall and free-slip rigid top wall) by finite-size particles, with a particle-to-fluid density ratio of 1.05 and a much lower volume fraction [$O(10^{-3})$]. The flow friction Reynolds number in their simulation was smaller (85.4). For $a_p/H = 0.05$, they found also that the presence of solid particles reduced the mean flow and the reduction occurs mostly in the transition region between the linear viscous sublayer and logarithmic inertial sublayer. For $a_p/H = 0.10$, however, they found that the mean flow is augmented very close to the wall ($y^+ < 7$), which is not the case in our LBM and FDDF simulations.

Another relevant study is the particle-resolved simulation of turbulent particle-laden channel by Uhlmann [16] (hereafter Uhlmann08), where he considered a case of $a_p/H = 0.025$, $\rho_p/\rho = 2.21$, $\phi_V = 0.0042$, and a friction Reynolds number of 172 (similar to ours). His density ratio is higher and volume fraction is lower. Since he considered a vertical channel and the potential energy change is larger in the particle-laden flow (due to $\rho_p/\rho > 1$), the friction Reynolds number in the particle-laden flow reached 225. This density difference makes it difficult to compare their profiles directly to our results here. So the comparison will be mainly restricted to the particle volume fraction profile.

To better quantify the modulation of the mean flow velocity by the presence of solid particles, we compare changes in the mean flow velocity relative to the single-phase flow in Fig. 7. Due to the change of resolution, the y^+ positions for the single-phase flow simulation could be different from the locations where the particle-laden flow data are computed. A linear interpolation is used to interpolate the particle-laden flow data to match the same locations used for the single-phase flow. The relative changes are always computed based on results of the single-phase and particle-laden flows using a same domain size and same computational approach. The computed relative changes of the local mean flow velocity from the LBM simulations are qualitatively similar to the FDDF data. Specifically, the locations of maximum reduction are the same and appear to only depend on the particle size.

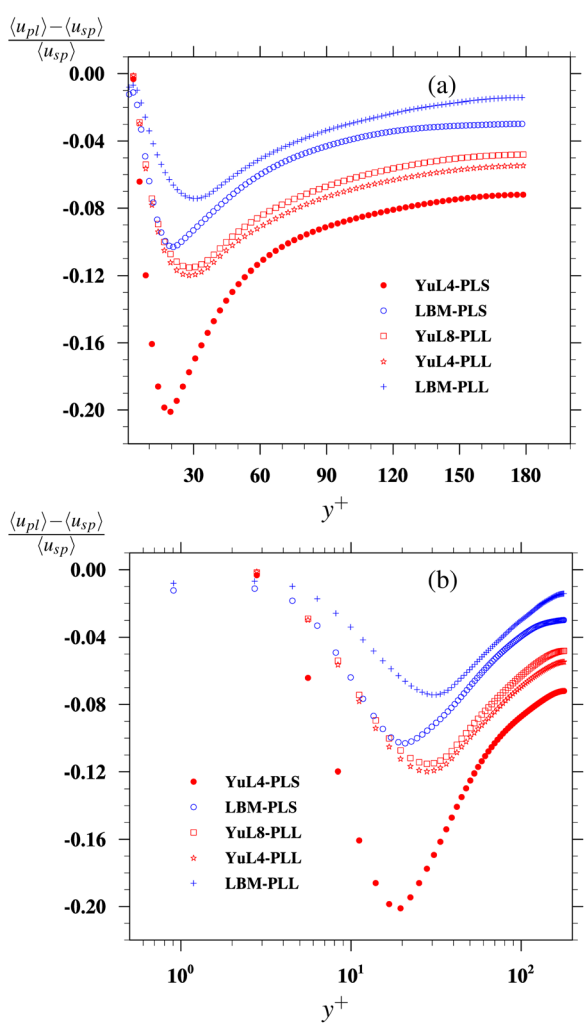

Fig. 7 The relative change in the mean velocity of the flow due to the presence of particles: (*a*) linear–linear plot and (*b*) log–linear plot

Both approaches show that the reduction is larger for the smaller particle size. Quantitatively, the LBM simulations yield significantly less reduction in the mean flow velocity at almost all locations. For the large particles, the maximum change in the mean flow velocity occurs at $y^+ \approx 30$, the reduction is 7.5% in LBM–PLL, 11.96% in YuL4–PLL, and 11.53% in YuL8–PLL. For the small particles, the maximum change in the mean flow velocity occurs at $y^+ \approx 21$, the reduction is 10.3% in LBM–PLS and 20.1% in YuL4–PLS. The location of maximum reduction appears to be correlated with the location of local particle volume fraction maximum (see Fig. 13). A comparison of results from YuL4–PLL and YuL8–PLL shows that the effect of domain size on this relative reduction is not significant. The difference between the two computational approaches originated from a combination of a slightly larger mean flow velocity for the single-phase flow and a slightly smaller mean velocity in the particle-laden case in the FDDF results (see Fig. 6). We suspect that the reason for this difference is related to the poor resolution of the boundary layer in FDDF (see the last column of Table 1). The first grid cell near the wall in FDDF is 2.81 wall units, which exceeds the maximum allowed value of 1.5 to 2 wall units recommended in Ref. [41]. In LBM, the near-wall resolution is 1.81 wall units. This combined with lower numerical dissipation and better rotational symmetry in LBM implies that the LBM results are likely more accurate.

It appears that there is always an inertial-sublayer region where the mean velocity can be fitted by $U^+ = \ln y^+/k + A$. In Fig. 8, we apply linear regression to the region $30 < y^+ < 130$. For the LBM–PLL run, we obtain $k = 0.326$ and $A = 2.411$ with a R^2 value (a measure of goodness-of-fit) of 1.0; while for the LBM–PLS run, we obtain $k = 0.326$ and $A = 2.237$ with a R^2 value of 0.9997. They can be compared to the values for the single-phase flow: $k = 0.40$ and $A = 5.5$. A smaller k implies a large slope in the log–linear plot. A smaller A means that the interception level with a vertical line at $y^+ = 1$ is reduced. The presence of solid particles makes the transition from the linear viscous sublayer to the logarithmic inertial sublayer more gradual. Interestingly, the k value for the two particle sizes happens to be identical.

We note that a recent study by Picano et al. [59] also considered neutrally buoyant solid particles in a turbulent channel. They used

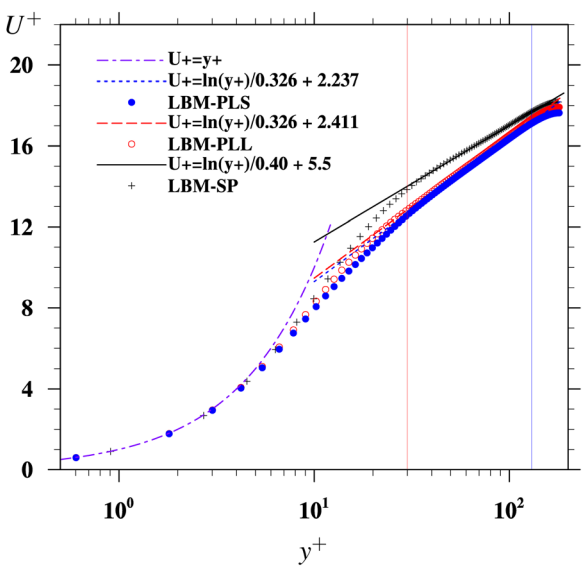

Fig. 8 The mean velocity profiles from the LBM simulations and fitting coefficients in the inertial sublayer by the logarithmic law. The two vertical lines mark the region where linear regression is performed to obtain a fit of the form $U^+ = \ln y^+/k + A$. The two vertical lines mark the region ($30 < y^+ < 130$) used to perform the logarithmic fitting.

a second-order finite-difference scheme on a staggered grid, with a domain size of $6H \times 2H \times 3H$ resolved by a $864 \times 288 \times 432$ grid. They applied the immersed boundary method to treat the moving fluid–solid interface. One of the cases they simulated has $\phi_V = 0.10$ and $a_p/H = 1/18 = 0.056$; these parameters are similar to our small-particle case LBM–PLS. They found the constants for the logarithmic region to be $k = 0.32$ and $A = 0.27$, so their slope and our slope for particle-laden flow are very similar.

The RMS velocity profiles from the LBM runs are compared in Fig. 9 on both linear–linear and log–linear plots. The general features shared by both particle sizes include: (1) in the streamwise direction, the presence of particles reduces the RMS velocity significantly in the near wall region but may increase the RMS velocity in the center region and (2) in the spanwise and transverse directions, the presence of solid particles has an opposite effect, namely, suppression of RMS velocity in the center region and augmentation of RMS velocity in the near-wall region. The level of these modulations is larger for smaller particles, perhaps due to a larger solid–fluid interface area per unit volume. The interface area per unit volume can be written as $S_{sf}/V = n4\pi a^2 = 3\phi_V/a_p$, so the PLS case has twice of the interface area of the PLL case. The RMS velocity profiles from the FDDF runs are shown in Fig. 10. The general features are very similar to that of Fig. 9.

In Figs. 11 and 12, we show the percentages of change of RMS velocity relative to the single-phase flow, for the LBM runs and FDDF runs, respectively. First, in the streamwise direction, the two approaches yield very similar quantitative results in most of

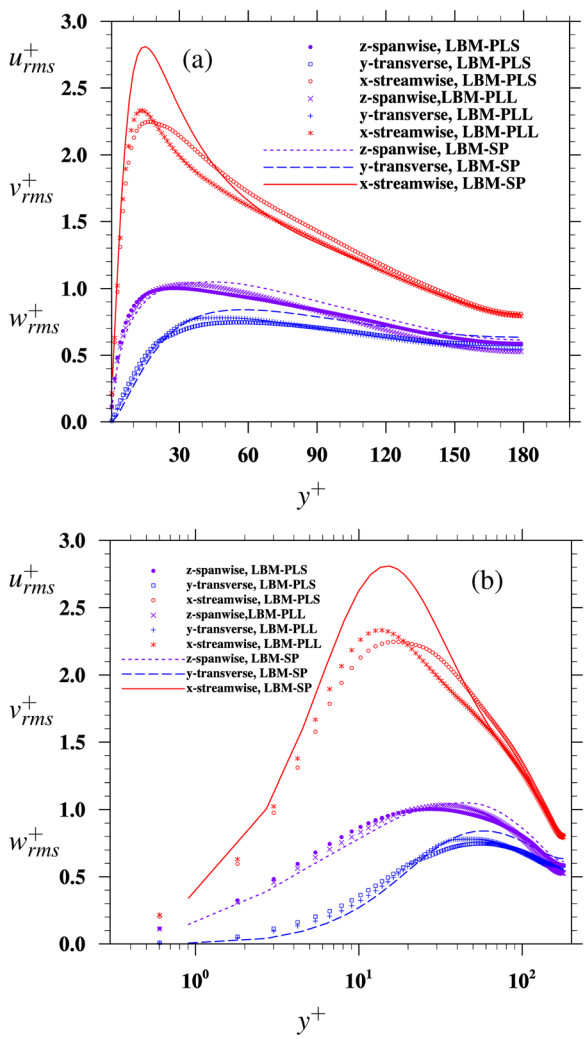

Fig. 9 The RMS velocity profiles in the flows simulated by LBM: (*a*) linear–linear plot and (*b*) log–linear plot

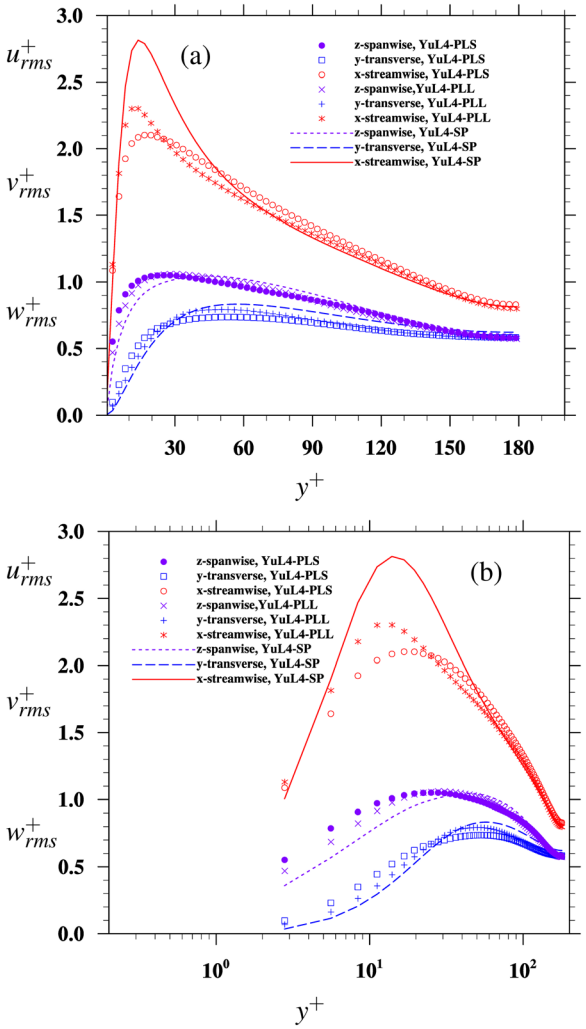

Fig. 10 The RMS velocity profiles in the flows simulated by the FDDF approach: (*a*) linear–linear plot and (*b*) log–linear plot

the channel, except very close to the wall where the LBM runs show reduction all the way to the wall, but the FDDF runs show augmentation immediately next to the wall. In general, there is a strong minimum (the largest reduction): 18.2% at $y^+ = 19.9$ for LBM–PLL, 19.2% at $y^+ = 19.6$ for YuL4–PLL, 17.9% at $y^+ = 19.6$ for YuL8–PLL, 20.4% at $y^+ = 13.6$ for LBM–PLS, and 25.9% at $y^+ = 14.0$ for YuL4–PLS. There is also a weak maximum (the moderate augmentation) within the inertial sublayer: 1.5% at $y^+ = 84.1$ for LBM–PLL, 2.8% at $y^+ = 120$ for YuL4–PLL, 2.1% at $y^+ = 117$ for YuL8–PLL, 6.9% at $y^+ = 82.3$ for LBM–PLS, and 6.4% at $y^+ = 93.5$ for YuL4–PLS. The difference between YuL4–PLL and YuL8–PLL runs is not significant.

Second, in the spanwise and transverse directions, the strongest modulations occur near the wall. The presence of particles augments the transverse RMS velocity by as much as 50%. The near-wall augmentations in the spanwise direction are 10–15% for the LBM runs and 30–50% for the FDDF runs; thus, they are quantitatively different. In the center region, the quantitative comparison is better, showing about 5–15% suppression. It should be noted that while both approaches show general agreement on the trends of turbulence modulation, the data contain some uncertainties due to limited time intervals that are used to obtain the average statistics.

In general, the quantitative agreement between LBM and YuL4 is much better in the RMS velocities (Figs. 9 and 10) and their relative changes (Figs. 11 and 12) due to presence of the solid particles, than in the mean velocity (Fig. 6) and its relative change

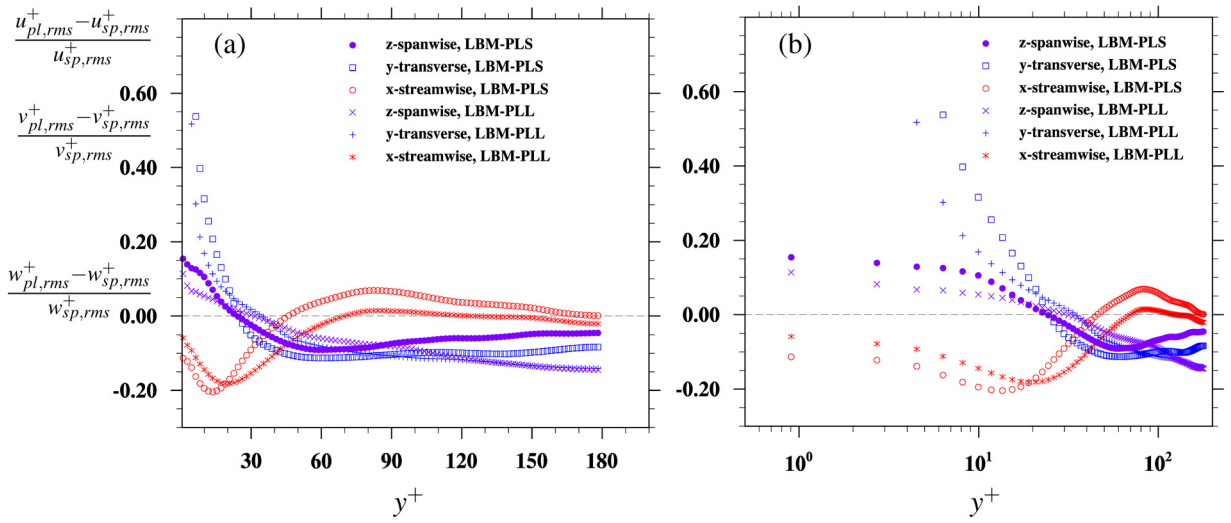

Fig. 11 The relative changes of RMS velocity fluctuations due to the presence of solid particles in the LBM simulations, relative to the single-phase flow simulated by the same method using a same domain size: (*a*) linear–linear plot and (*b*) log–linear plot

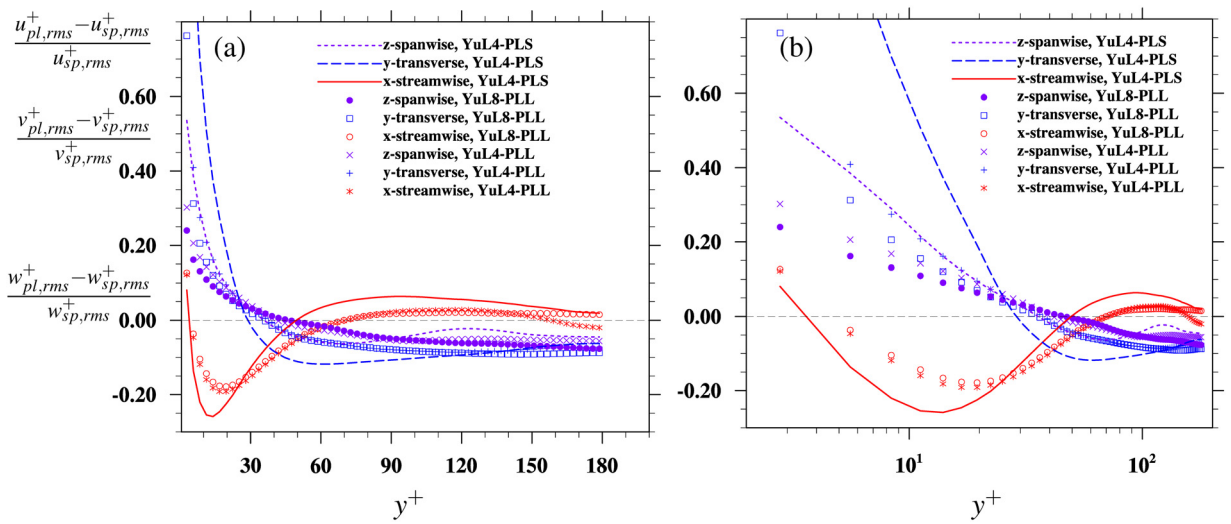

Fig. 12 The relative changes of RMS velocity fluctuations due to the presence of solid particles in the FDDF simulations, relative to the single-phase flow simulated by the same method using a same domain size: (*a*) linear–linear plot and (*b*) log–linear plot

(Fig. 7). This general agreement is very encouraging due to the very different methods (mesoscopic lattice Boltzmann versus macroscopic N–S) used to simulate the flow, and the very different methods used to treat the fluid-moving solid interfaces (mesoscopic bounce back versus macroscopic direct forcing). For such complex flows where microscopic measurements at the scale of solid particle size are hard to obtain, establishing such intercomparison between the two different approaches will open ways to gather reliable statistics at both the channel scale and the particle size scale (e.g., statistics conditioned on the particle surface [23]).

We may compare our results (LBM–PLL, YuL4–PLL, and YuL8–PLL) with $a_p/H = 0.05$ and $\rho_p/\rho = 1$ to the results of PB97 with $a_p/H = 0.05$ and $\rho_p/\rho = 1.05$ (Fig. 14(*a*) in PB97). Their results for the transverse (wall-normal) direction are qualitatively the same, with augmentation near the wall, followed by reduction further away from the wall. However, their results show that the spanwise RMS velocity is always augmented by the presence of the particles, and the streamwise RMS velocity is augmented immediately to the right of its peak location. Since their treatments of fluid-moving particle interfaces are not exact, we believe our LBM and FDDF results are much more accurate and reliable.

3.2.2 Particle Distribution and Particle Phase-Averaged Mean Velocity. As indicated in the above discussions, to the lowest order, the particle volume percentage distribution $\Psi(y)$ and particle mean velocity $U_p^+(y)$ are relevant. Here, we shall discuss them briefly, a full exposition of the statistics related to the particulate phase is beyond the scope of this current paper.

It has been well known that small inertial particles may accumulate in low-speed streaks in the viscous sublayer [60]. The current problem is very different: particles have no relative inertia, but there are of finite sizes so the disturbance flows around the particles contain inertial effects. In a laminar wall-bounded flow at low particle volume fraction, it is well known that at a finite-size particle may find certain (single or multiple) equilibrium positions between the center and the wall, known as the Segré–Silberberg effect [61,62]. This results from a balance of the

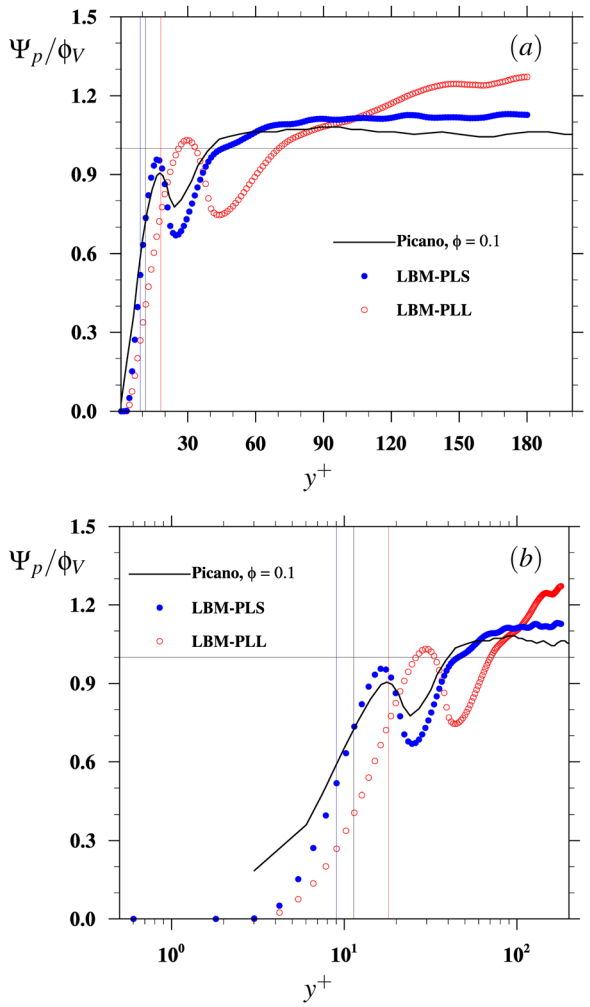

Fig. 13 The average local volume fraction Ψ_p of the particulate phase as a function of y^+: (*a*) linear–linear plot and (*b*) log–linear plot. The profile from Picano et al. [59] at $\phi_V = 0.1$ and $a_p/H = 1/18 = 0.056$ is also shown for comparison. The vertical lines mark the location of $y = a_p$.

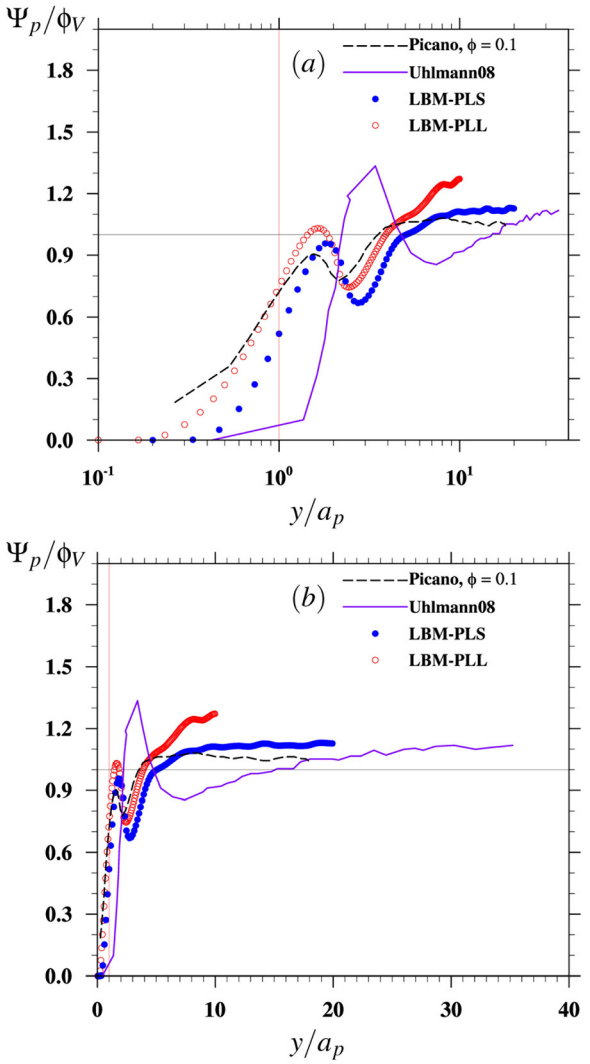

Fig. 14 Replot of Fig. 13 as a function of y/a_p: (*a*) log–linear plot and (*b*) linear–linear plot. The profiles from Uhlmann [16] and Picano et al. [59] are also shown for comparison.

inertia-induced lift force and lubrication force due to the wall. Even for the simplest case of neutrally buoyant particles, the equilibrium positions depend on the flow Reynolds number and the particle size. This Segré–Silberberg effect is also affected by the local hydrodynamic interaction between solid particles, see further discussions and references of the Segré–Silberberg effect in Ref. [63].

An interesting question here is whether the solid particles are distributed uniformly or clustered near the wall. Figure 13 shows $\Psi_n \equiv \Psi_p/\phi_V$ as a function of y^+. Due to the finite size, Ψ_p is zero at $y^+ = 0$. The vertical thin line marks the location of $y = a_p$. For the large case (LBM–PLL), Ψ_n increases near the wall and reaches a maximum that is 1.031, at $y/a_p = 1.64$ or $y^+ = 29.50$. It then decreases and reaches a minimum of 0.745, at $y/a_p = 2.44$ or $y^+ = 43.95$. There is a very gradual increase in ϕ_n, when y^+ is increased from 44 to 120. In the center region ($y^+ > 120$), ϕ_n is nearly uniform and is 1.234. For the small particle case (LBM–PLS), the first peak from the wall has a value of 0.956 reached at $y/a_p = 1.80$ ($y^+ = 16.25$) and the minimum 0.674 reached at $y/a_p = 2.74$ ($y^+ = 24.7$). The key difference between the large and small particles is in the center region: for the small particle case, the volume fraction is more or less uniform for $y^+ > 60$, while for the large particle case it is slowly increasing with y^+.

Also shown in Fig. 13 is the profile from Picano et al. [59] with $\phi_V = 0.10$ and $a_p/H = 1/18 = 0.056$. Since they fixed the mean bulk velocity, the friction Reynolds number was 153. Despite the differences in numerical method, volume fraction, particle size, etc., the local volume fraction profile is qualitative similar to our LBM–PLS profile: a maximum near the wall followed by a minimum and a constant value in the channel center region. The center-region volume fraction is also larger than the mean value. Note that in all our plots, the friction velocity in the single-phase flow was used to define the wall units.

The Ψ_n profiles are replotted as a function of y/a_p in Fig. 14. The data from Uhlmann08 for the case of $a_p/H = 0.025$, $\rho_p/\rho = 2.21$, and $\phi_V = 0.0042$ are added for comparison. The profile from Picano et al. [59] with $\phi_V = 0.10$ and $a_p/H = 0.056$ is also plotted. We observe that the Ψ_n profiles are more similar, implying that the locations of the near-wall maximum and minimum scale better with the particle size. The curve from Uhlmann08 is qualitatively similar, with a near-wall maximum followed by a minimum and then gradual increase toward the center of the channel. However, perhaps due to the higher particle inertia, the location of the near-wall maximum and minimum is shifted away from the wall. The near-wall maximum also has a larger magnitude. The general conclusion is that the volume fraction distribution is nonmonotonic.

The location of the near-wall maximum could be interpreted as a quasi-equilibrium position and is located at $y = 1.64a_p$ (larger particles) to $1.80a_p$ (small particles), thus very close to the wall.

We argue that this quasi-equilibrium is similar to the Segré–Silberberg effect [61,62]. This is confirmed by the hydrodynamic force and total force (hydrodynamic plus the lubrication force) in the transverse direction, shown in Fig. 15, as a function of the center position of the solid particles (using two normalizations for the distance). Here, the center positions of the solid particles are divided into bins of width $\Delta y^+ \approx 3.5$, and the average force is computed by averaging over all particles with the centers sitting in a given bin. A positive force denotes a force directed away from the wall and negative into the wall. Note that Fig. 15(*b*) shows all the data near the channel wall, while Fig. 15(*a*) uses a narrow y range in order to better show the behavior near the channel center. The lubrication force includes the repulsive forces due to both the particle–particle and particle–wall interactions.

First, in each case (LBM–PLL and LBM–PLS), in the first bin next to the wall with particles, the hydrodynamic force is close to zero (implying these particles have very low velocities); but the lubrication force (based on the simple model) due to the wall generates a large force away from the wall, which will push the solid particle back into the bulk flow. Immediately outside (the next few bins after the first nontrivial bin), the hydrodynamic force is negative, implying that the particles move away from the wall. The net lubrication force also changes direction and becomes negative, this is primarily due to the outward movement, but the particle–particle hydrodynamic interaction (which is biased as more particles are located to the right if the wall is on the left) may also contribute to this change. The net force crosses zero at $y^+ = 29.50$ $(y/a_p = 1.64)$ and $y^+ = 18.6$ $(y/a_p = 2.0)$ for LBM–PLL and LBM–PLS, respectively. These locations correspond roughly to the location of maximum Ψ_p. At the location of net zero force, the hydrodynamic force is now positive. There is a region $(29.5 < y^+ < 65$ for large particles and $18.1 < y^+ < 37.0$ for small particles) where the net force is positive, and in this region particles on average migrate toward to the center region of the channel. The location $y^+ < 65$ (for large particles) or $y^+ < 37$ (for small particles) could be interpolated as the second quasi-equilibrium position, but the exact location is vague due to large uncertainties (limited samples). Longer simulations are needed to obtain better curves. Finally, in the region $70 < y^+ < 150$, the net force appears to be weakly negative, with a weakly positive net lubrication force.

In Fig. 16, we plot the phase-partitioned mean velocity profiles (U^+ and U_p^+), which are velocity inside each phase, averaged over all lattice nodes within the respective phase at a given y location. The velocity inside a solid particle is given by the translation velocity at the particle center plus solid body rotation. U^+ data are the same as those shown in Fig. 6. The most interesting feature is that, very close to the wall, the particle mean speed is significantly larger than the fluid velocity, implying that there is a significant slip between the particle motion and the wall. A linear extrapolation shown in Fig. 16(*b*) shows that the effective slip is $8.80u^*$ and

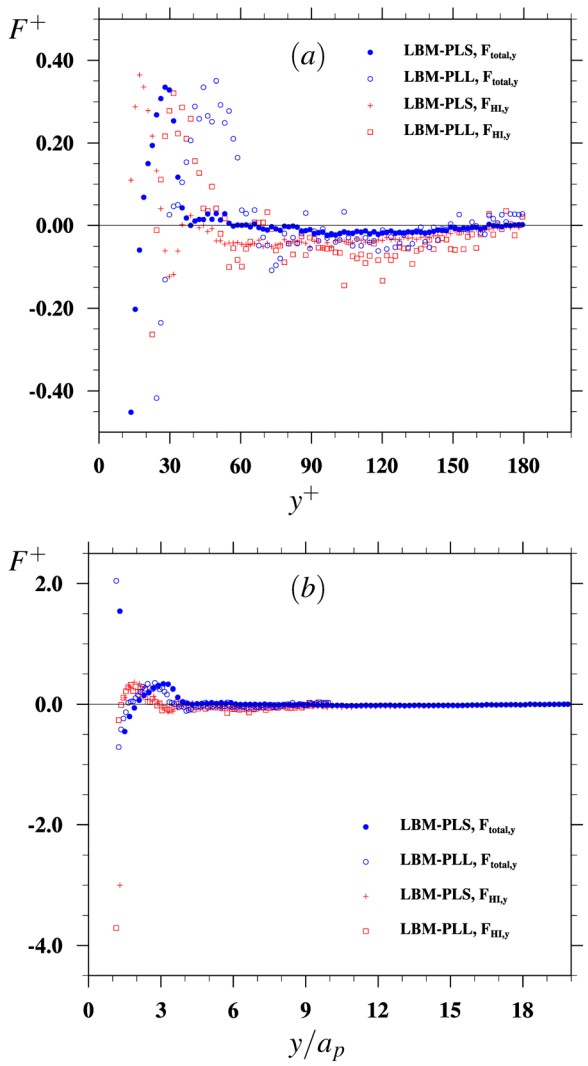

Fig. 15 The average forces normalized by $[\rho_f(u^*)^2 d_p^2]$, acting on the particle along the transverse direction as a function of (*a*) y^+ and (*b*) y/a_p

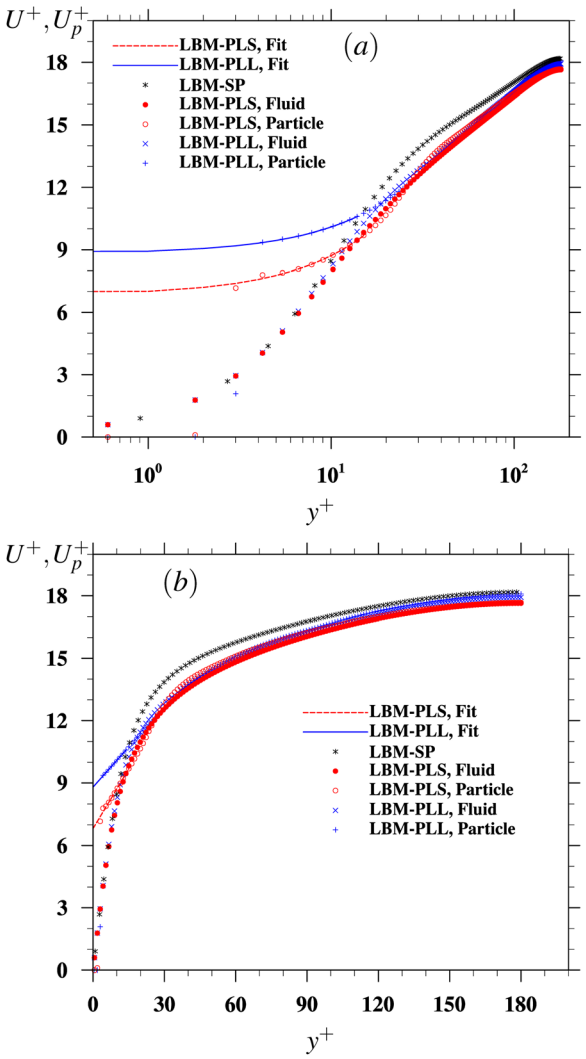

Fig. 16 Comparison of the phase-partitioned mean velocity profiles: (*a*) Log-linear plot and (*b*) linear-linear plot

$6.82u^*$ for large and small particles, respectively. In the intermediate region ($19.9 < y^+ < 46.4$ for LBM–PLL and $15.1 < y^+ < 24.7$ for LBM–PLS), the fluid velocity exceeds slightly the particle velocity. Then in the center region, they reach to mutual equilibrium, with particle velocity slightly large than the fluid velocity (about 0.9% for LBM–PLL and 0.7% for LBM–PLS). For the small particle case, there is a third region $24.68 < y^+ < 98.13$ where the mean velocity of particle again exceeds that of fluid by about 1%.

The phase-averaged particle mean speeds ($\overline{U}_p^+$) for LBM–PLL and LBM–PLS are 16.16 and 15.78, respectively. These are larger than the respective phase-averaged fluid mean speeds (15.02 for LBM–PLL and 14.82 for LBM–PLS) by 7.59% and 6.48%. This may be interpreted as the mean slip between the two phases. In fact, the phase-averaged particle mean speeds are larger than the single-phase mean flow speed (15.74). Substituting these into Eq. (22), we obtain $\overline{U^+} + [\phi_V/(1-\phi_V)][\rho_p/\rho]\overline{U_p^+} = 16.25$ for the large particle case and 16.02 for the small particle case. This implies that the fluid phase-averaged viscous dissipation is increased by $(16.25 - 15.74)/15.74 = 3.24\%$ for the large particle case and 1.88% for the small particle case, even though the fluid-phase mean speed is reduced relative to the single-phase flow.

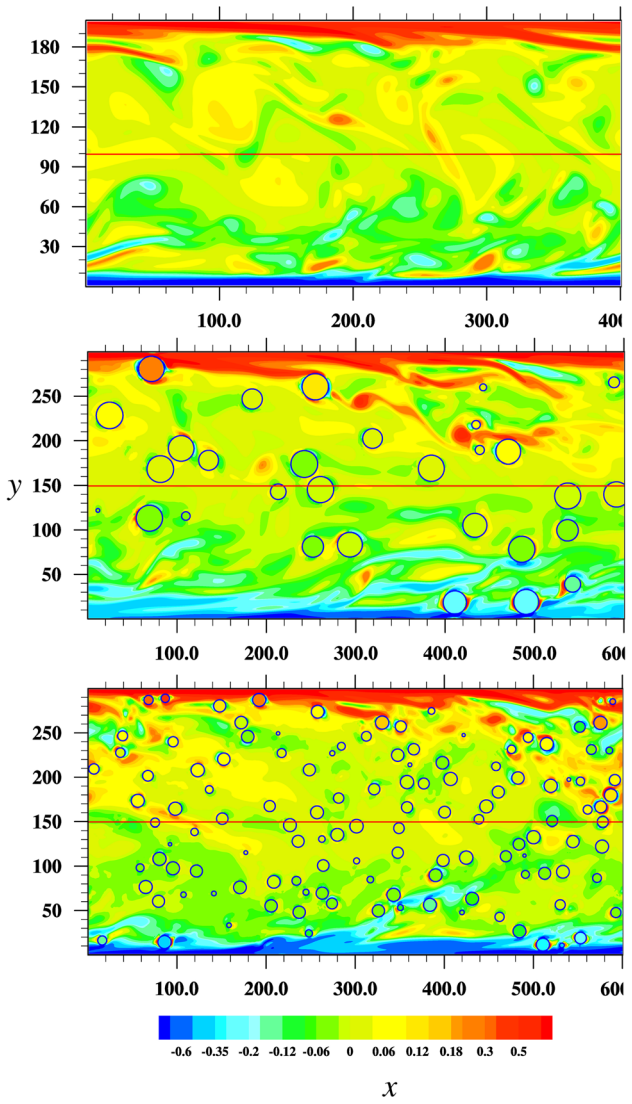

Fig. 17 Visualization of instantaneous spanwise vorticity ω_z, normalized by u^{*2}/ν, on an $x-y$ slice: (*a*) LBM–SP, (*b*) LBM–PLL, and (*c*) LBM–PLS

Finally, Fig. 17 provides visualization of the instantaneous spanwise vorticity ω_z, normalized by u^{*2}/ν, at the stationary stage from the LBM–SP, LBM–PLL, and LBM–PLS runs. The viscous boundary layers around solid particles are visible by local higher-than-average vorticity near the particle surfaces. The visualizations show that the near-wall vortices are being transported away (or being lifted up) from the wall due to the presence of the solid particles, indicating that solid particles stir the near-wall vortical structures and cause a higher-level of mixing or exchange of the flow between the near-wall region and the outside. Perhaps this explains why the strongest turbulence modulation occurs in the transition region between the linear viscous sublayer and the logarithmic inertial layer. Shao et al. [17] argued that the large-scale streamwise vortices are suppressed by added viscous dissipation due to solid particles entrained within and other particles outside large-scale vortices induce the smaller-scale structures, both hindering the development of the large-scale streamwise vortices.

4 Summary and Outlook

Motivated by the need to understand turbulence modulation by finite-size solid particles in a wall-bounded flow, in this paper, we reported the first particle-resolved simulations of turbulent particle-laden channel flow using the mesoscopic lattice Boltzmann approach. The effects of fluid-moving particle interfaces on the fluid motion are treated by an interpolated bounce-back scheme, and the effects on the dynamics of the solid particles (the hydrodynamic force/torque acting on a moving particle) are handled by a local Galilean-invariance momentum exchange method [42,50]. These treatments are fully consistent with the mesoscopic scheme and do not require any smoothing at the interfaces (as often encountered in the popular immersed boundary method). Thus, the method treats the fluid-moving solid particle interfaces as sharp interfaces and maintains the advantage of low numerical dissipation of the lattice Boltzmann approach. This is important for accurate particle-resolved DNS of turbulent particle-laden flows, where sharp velocity gradients occur near the moving solid surfaces. The sharp-interface treatment requires a sufficient grid resolution to be numerically stable, efforts are still needed to enhance the numerical stability of the approach. We have recently introduced a velocity-constrained normal extrapolation refilling to fill the missing populations at the new fluid nodes, and this method takes advantage of the MRT lattice Boltzmann approach and was found to improve numerical stability [42].

One main goal of the paper is to demonstrate that the results from the LBM approach are accurate and reliable. We first simulated the single-phase turbulent channel flow at $\mathrm{Re}_\tau = 180$. The resulting mean flow profile and turbulence statistics were found to be in excellent agreement with the published data based on the spectral method [57,58]. The results were also compared with a macroscopic FDDF approach. The RMS velocity profiles resulting from the LBM approach and the FDDF approach using the same domain size ($4H \times 2H \times 2H$) are in excellent agreement. The FDDF results show that the domain size affects the values of RMS velocities in the streamwise and spanwise directions.

We then considered a particle-laden turbulent channel flow under the same body force used to drive the single-phase flow. The particles have a same density as the fluid. Two particle sizes ($a_p = 0.1H$ and $0.05H$) were considered, with the overall particle volume fraction fixed at 7.1%. A systematic intercomparison between the LBM approach and the FDDF approach was performed. While there are some discrepancies between the simulated mean flow profiles, the two approaches yield quantitatively similar RMS velocity profiles for the particle-laden flows. Such direct intercomparisons under essentially identical conditions are rare, but are much needed to establish the fidelity of numerical methods and the resulting data. Given the higher grid resolution, lower numerical dissipation, and better rotational symmetry in LBM, we believe the LBM results are likely more accurate than the FDDF results.

We studied the flow modulations by finite-size particles in the turbulent channel flow and the effects of finite particle size. Under the same driving body force, we found that the mean flow speed was reduced by 4.6% and 5.8% due to the presence of the large and small particles, respectively, but the local phase-averaged flow dissipation was increased by 3.2% and 1.9%, respectively. This implies that the fluid–particle system is more dissipative than the single-phase flow. It was found that a logarithmic inertial sublayer still exists in the particle-laden flows for $30 < y^+ < 130$, but with a slope and interception that are different from the single-phase flow. A similar observation is made in a recent study by Picano et al. [59].

The key observations regarding modulation of the fluid RMS velocity include:

(1) The presence of the particulate phase strongly affects the RMS velocity fluctuations in the near wall region, and the level and nature of modulation depend on the spatial direction and location.
(2) In the streamwise direction, the RMS velocity is significantly reduced below the inertial sublayer and weakly augmented within the inertial sublayer.
(3) In the transverse and spanwise directions, the RMS velocities are increased below the inertial sublayer and are reduced in the inertial sublayer and the channel center.

Similar observations were made in Shao et al. [17], who concluded that the presence solid particles weakens the large-scale streamwise vortices and generates small-scale vortices. We argue from preliminary flow visualizations that solid particles enhance the mixing and exchange of fluid motion and vortices between the near wall region and the outside that region. The FDDF results showed that the relative changes due to the presence of particles are not sensitive to the computational domain size. One qualitative difference between the results from the two approaches concerns whether the streamwise RMS velocity is reduced or enhanced immediately next to the wall. The LBM results show reduction all the way to the wall, but the FDDF results show augmentation next to the wall.

The particle volume fraction was found to have an interesting nonmonotonic distribution. We found that there is a dynamic equilibrium location resembling the Segŕe–Silberberg effect known for a laminar wall-bounded flows [61,62]. This equilibrium location is very close to the wall (with particle center at roughly $2a_p$ away from the wall). We found that there is a finite slip at the channel wall for particle mean velocity ($8.80u^*$ for the large particles and $6.82u^*$ for the small particles, roughly half of the mean flow speed) between the particle mean motion and the channel wall, and the slip is larger for large particles. Such strong slip implies that solid particles do not stay in the near-wall region for too long. The phase-averaged particle mean speed was also larger than the mean fluid speed as a result of this slip.

In summary, this study established a mesoscopic computational approach for particle-laden turbulent flows. Significant flow modulations were found on the RMS velocities due to the presence of particles, even for neutrally buoyant particles. The effects of finite particle size are reflected in the level and location of flow modulation, as well as in the volume fraction distribution and particle slip velocity near the wall. In some cases, a longer simulation would be desired to obtain better flow statistics. The lubrication force model may affect the simulated results, which needs further investigation. The analyses presented in this paper should be considered preliminary. The parameter space for the particle-laden flow system is large, and substantial efforts are needed to cover this space and to compare with experimental results in the literature. Also rigorous theoretical modeling methods are needed to help interpret the simulation results.

Acknowledgment

This work has been supported by the U.S. National Science Foundation (NSF) under Grants Nos. CBET-1235974 and AGS-1139743 and by the Air Force Office of Scientific Research under Grant No. FA9550-13-1-0213. L. P. W also acknowledges the support from the Ministry of Education of the People's Republic of China and the Huazhong University of Science and Technology through Chang Jiang Scholar Visiting Professorship. Z. Y. acknowledges the support from the National Natural Science Foundation of China (No. 11372275). Computing resources are provided by the National Center for Atmospheric Research through CISL-P35751014 and CISL-UDEL0001 and by the University of Delaware through NSF CRI 0958512.

Nomenclature

a_p = radius of solid particles
c_s = speed of sound
d_p = diameter of solid particles
$\mathbf{e}$ = microscopic velocity
$\mathbf{f}$ = microscopic distribution function vector
$\mathbf{F}$ = force acting on a particle
g = body force per unit mass
H = half width of the channel
I_p = moment of inertia of a particle
L_x = computational domain size in the streamwise (x) direction
L_y = computational domain size in the wall-normal or transverse (y) direction
L_z = computational domain size in the spanwise (z) direction
$\mathbf{m}$ = microscopic moments vector
$\mathbf{M}$ = transformation matrix from $\mathbf{f}$ to $\mathbf{m}$
M_p = mass of a solid particle
n = particle number density
N = number of grid points in a given spatial direction
N_p = the total number of solid particles in the computational domain
p = local fluid pressure
P = phase-averaged fluid pressure at a given y
$\mathbf{q}$ = nonuniform force vector per unit mass
$\mathbf{Q}$ = nonuniform force vector in the microscopic velocity space
Re_τ = Reynolds number based on the friction velocity, $\mathrm{Re}_\tau = Hu^*/\nu$
$\mathbf{S}$ = relaxation matrix
$\mathbf{T}$ = torque acting on a particle
u = fluid velocity in the x-direction
$\overline{U}$ = phase-averaged fluid velocity over the whole volume
u^* = friction velocity
$U(y)$ = phase-averaged fluid velocity at a given y
$U_p(y)$ = phase-averaged solid velocity at a given y
$\overline{U_p}$ = phase-averaged solid velocity over the whole volume
v = fluid velocity in the y-direction
$\mathbf{V}$ = particle velocity
w = fluid velocity in the z-direction
$\mathbf{Y}$ = particle position
δt = time step size
δy = grid length in the y-direction
$\delta\rho$ = density fluctuations in LBM
η = wall length unit ($\eta = \nu/u^*$) or Kolmogorov scale
Θ = particle angular position
ν = fluid kinematic viscosity
ρ = fluid density
ρ_p = density of solid particles
τ_w = wall shear stress
ϕ_V = average particle volume fraction
Ψ = local average volume fraction at a given y
Ω_p = particle angular velocity

Subscripts

i, j = spatial direction indices
p = solid or the particulate phase

pl = quantities associated with a particle-laden flow
RMS = root-mean-squared value
sp = quantities associated with a single-phase flow
α = microscopic lattice-velocity direction, from 0 to 18

Superscripts

$^{-1}$ = inverse matrix
$^{(eq)}$ = value corresponding to equilibrium
$^{+}$ = normalized quantities in wall units
* = quantities normalized by the friction velocity
$'$ = the fluctuation component in the Reynolds decomposition

References

[1] Corsini, A., Rispoli, F., Sheard, A. G., and Venturini, P., 2013, "Numerical Simulation of Coal Fly-Ash Erosion in an Induced Draft Fan," ASME J. Fluids Eng., **135**(1), p. 081303.
[2] Patro, P., and Dash, S. K., 2014, "Computations of Particle-Laden Turbulent Jet Flows Based on Eulerian Model," ASME J. Fluids Eng., **136**(1), p. 011301.
[3] Balachandar, S., and Eaton, J. K., 2010, "Turbulent Dispersed Multiphase Flow," Annu. Rev. Fluid Mech., **42**(1), pp. 111–133.
[4] Maxey, M. R., and Riley, J. J., 1983, "Equation of Motion for a Small Rigid Sphere in a Nonuniform Flow," Phys. Fluids, **26**(4), pp. 883–889.
[5] Wang, L.-P., Rosa, B., Gao, H., He, G. W., and Jin, G. D., 2009, "Turbulent Collision of Inertial Particles: Point-Particle Based, Hybrid Simulations and Beyond," Int. J. Multiphase Flow, **35**(9), pp. 854–867.
[6] Squires, K. D., and Eaton, J. K., 1991, "Preferential Concentration of Particles by Turbulence," Phys. Fluids A, **3**(5), pp. 1169–1179.
[7] Wang, L.-P., and Maxey, M. R., 1993, "Settling Velocity and Concentration Distribution of Heavy Particles in Homogeneous Isotropic Turbulence," J. Fluid Mech., **256**, pp. 27–68.
[8] Squires, K. D., and Eaton, J. D., 1990, "Particle Response and Turbulence Modification in Isotropic Turbulence," Phys. Fluids A, **2**(7), pp. 1191–1203.
[9] Elghobashi, S., and Truesdell, G., 1993, "On the 2-Way Interaction Between Homogeneous Turbulence and Dispersed Solid Particles. I: Turbulence Modification," Phys. Fluids A, **5**(7), pp. 1790–1801.
[10] Sundaram, S., and Collins, L. R., 1997, "Collision Statistics in an Isotropic Particle-Laden Turbulent Suspension. Part 1—Direct Numerical Simulations," J. Fluid Mech., **335**, pp. 75–109.
[11] Zhou, Y., Wexler, A. S., and Wang, L.-P., 2001, "Modeling Turbulent Collision of Bidisperse Inertial Particles," J. Fluid Mech., **433**, pp. 77–104.
[12] Ayala, O., Grabowski, W. W., and Wang, L.-P., 2007, "A Hybrid Approach for Simulating Turbulent Collisions of Hydrodynamically-Interacting Particles," J. Comput. Phys., **225**(1), pp. 51–73.
[13] Jin, G. D., He, G. W., and Wang, L.-P., 2010, "Large Eddy Simulation of Collisional Statistics of Inertial Particles in Isotropic Turbulence," Phys. Fluids., **22**(5), p. 055106.
[14] Burton, T. M., and Eaton, J. K., 2005, "Fully Resolved Simulations of Particle–Turbulence Interaction," J. Fluid Mech., **545**, pp. 67–111.
[15] Uhlmann, M., 2005, "An Immersed Boundary Method With Direct Forcing for the Simulation of Particulate Flows," J. Comput. Phys. **209**(2), pp. 448–476.
[16] Uhlmann, M., 2008, "Interface-Resolved Direct Numerical Simulation of Vertical Particulate Channel Flow in the Turbulent Regime," Phys. Fluids, **20**(5), p. 053305.
[17] Shao, X., Wu, T., and Yu, Z., 2012, "Fully Resolved Numerical Simulation of Particle-Laden Turbulent Flow in a Horizontal Channel at a Low Reynolds Number," J. Fluid Mech., **693**, pp. 319–344.
[18] Yang, J. M., and Stern, F., 2014, "A Sharp Interface Direct Forcing Immersed Boundary Approach for Fully Resolved Simulations of Particulate Flows," ASME J. Fluids Eng., **136**(4), p. 040904.
[19] Zhang, Z., and Prosperetti, A., 2005, "A Second-Order Method for Three-Dimensional Particle Simulation," J. Comput. Phys., **210**(1), pp. 292–324.
[20] Yeo, K., Dong, S., Climent, E., and Maxey, M. R., 2010, "Modulation of Homogeneous Turbulence Seeded With Finite Size Bubbles or Particles," Int. J. Multiphase Flow, **36**(3), pp. 221–233.
[21] Homann, H., and Bec, J., 2010, "Finite-Size Effects in the Dynamics of Neutrally Buoyant Particles in Turbulent Flow," J. Fluid Mech., **651**, pp. 81–91.
[22] Gao, H., Li, H., and Wang, L.-P., 2013, "Lattice Boltzmann Simulation of Turbulent Flow Laden With Finite-Size Particles," Comput. Math. Appl., **65**(2), pp. 194–210.
[23] Wang, L.-P., Ayala, O., Gao, H., Andersen, C., and Mathews, K., 2014, "Study of Forced Turbulence and Its Modulation by Finite-Size Solid Particles Using the Lattice Boltzmann Approach," Comput. Math. Appl., **67**(2), pp. 363–380.
[24] Gillissen, J., 2013, "Turbulent Drag Reduction Using Fluid Spheres," J. Fluid Mech., **716**, pp. 83–95.
[25] Ten Cate, A., Derksen, J. J., Portela, L. M., and van den Akker, H. E. A., 2004, "Fully Resolved Simulations of Colliding Monodisperse Spheres in Forced Isotropic Turbulence," J. Fluid Mech., **519**, pp. 233–271.
[26] Ernst, M., Dietzel, M., and Sommerfeld, M., 2013, "A Lattice Boltzmann Method for Simulating Transport and Agglomeration of Resolved Particles," Acta Mech., **224**(10), pp. 2425–2449.
[27] Pan, Y., and Banerjee, S., 1997, "Numerical Investigation of the Effects of Large Particles on Wall Turbulence," Phys. Fluids, **9**(12), pp. 3786–3807.
[28] Vowinckel, B., Kempe, T., and Froehlich, J., 2014, "Fluid–Particle Interaction in Turbulent Open Channel Flow With Fully-Resolved Mobile Beds," Adv. Water Resour., **72**, pp. 32–44.
[29] Rashidi, M., Hetstoni, G., and Banerjee, S., 1990, "Particle Turbulence Interaction in a Boundary Layer," Int. J. Multiphase Flow, **16**(6), pp. 935–949.
[30] Kaftori, D., Hetsroni, G., and Banerjee, S., 1998, "The Effect of Particles on Wall Turbulence," Int. J. Multiphase Flow, **24**(3), pp. 359–386.
[31] Rogers, C. B., and Eaton, J. K., 1991, "The Effect of Small Particles on Fluid Turbulence in a Flat-Plate, Turbulent Boundary Layer in Air," Phys. Fluids, **3**(5), pp. 928–937.
[32] Zisselmar, R., and Molerus, O., 1979, "Investigation of Solid–Liquid Pipe Flow With Regard to Turbulence Modification," Chem. Eng. J., **18**(3), pp. 233–239.
[33] Belt, R. J., Daalmans, A. C. L. M., and Portela, M., 2012, "Experimental Study of Particle-Driven Secondary Flow in Turbulent Pipe Flows," J. Fluid Mech., **709**, pp. 1–36.
[34] Gore, R. A., and Crowe, C. T., 1989, "Effect of Particle Size on Modulating Turbulent Intensity," Int. J. Multiphase Flow, **15**(2), pp. 279–285.
[35] Hetsroni, G., 1989, "Particle Turbulence Interaction," Int. J. Multiphase Flow, **15**(5), pp. 735–746.
[36] Matas, J. P., Morris, J. F., and Guazzelli, E., 2003, "Transition to Turbulence in Particulate Pipe Flow," Phys. Rev. Lett., **90**(1), p. 014501.
[37] Yu, Z., and Shao, X., 2007, "A Direct-Forcing Fictitious Domain Method for Particulate Flows," J. Comput. Phys., **227**(1), pp. 292–314.
[38] Chen, S., and Doolen, G., 1998, "Lattice Boltzmann Method for Fluid Flows," Annu. Rev. Fluid Mech., **30**(1), pp. 329–364.
[39] Qian, Y. H., d'Humières, D., and Lallemand, P., 1992, "Lattice BGK Models for Navier–Stokes Equation," Europhys. Lett., **17**(6BIS), pp. 479–484.
[40] Peng, Y., Liao, W., Luo, L.-S., and Wang, L.-P., 2010, "Comparison of the Lattice Boltzmann and Pseudo-Spectral Methods for Decaying Turbulence: Low-Order Statistics," Comput. Fluids, **39**(4), pp. 568–591.
[41] Lammers, P., Beronov, K. N., Volkert, R., Brenner, G., and Durst, F., 2006, "Lattice BGK Direct Numerical Simulation of Fully Developed Turbulence in Incompressible Plane Channel Flow," Comput. Fluids, **35**(10), pp. 1137–1153.
[42] Peng, C., Teng, Y., Hwang, B., Guo, Z., and Wang, L.-P., 2015, "Implementation Issues and Benchmarking of Lattice Boltzmann Method for Moving Particle Simulations in a Viscous Flow," Comput. Math. Appl. (in press).
[43] d'Humières, D., Ginzburg, I., Krafczyk, M., Lallemand, P., and Luo, L.-S., 2002, "Multiple-Relaxation-Time Lattice Boltzmann Models in Three-Dimensions," Philos. Trans. R. Soc. London A, **360**(1792), pp. 437–451.
[44] Guo, Z., Zheng, C., and Shi, B., 2002, "Discrete Lattice Effects on the Forcing Term in the Lattice Boltzmann Method," Phys. Rev. E., **65**(4), p. 046308.
[45] Lu, J., Han, H., Shi, B., and Guo, Z., 2012, "Immersed Boundary Lattice Boltzmann Model Based on Multiple Relaxation Times," Phys. Rev. E., **85**(1), p. 016711.
[46] He, X., and Luo, L.-S., 1997, "Theory of the Lattice Boltzmann Method: From the Boltzmann Equation to the Lattice Boltzmann Equation," Phys. Rev. E., **56**(6), pp. 6811–6817.
[47] Shan, X. W., Yuan, X. F., and Chen, H. D., 2006, "Kinetic Theory Representation of Hydrodynamics: A Way Beyond the Navier–Stokes Equation," J. Fluid Mech., **550**, pp. 413–441.
[48] Lallemand, P., and Luo, L.-S., 2003, "Lattice Boltzmann Method for Moving Boundaries," J. Comput. Phys., **184**(2), pp. 406–421.
[49] Caiazzo, A., 2008, "Analysis of Lattice Boltzmann Nodes Initialisation in Moving Boundary Problems," Prog. Comput. Fluid Dyn., **8**(1–4), pp. 3–10.
[50] Wen, B., Zhang, C., Tu, Y., Wang, C., and Fang, H., 2014, "Galilean Invariant Fluid–Solid Interfacial Dynamics in Lattice Boltzmann Simulations," J. Comput. Phys., **266**, pp. 161–170.
[51] Nguyen, N. Q., and Ladd, A. J. C., 2002, "Lubrication Corrections for Lattice-Boltzmann Simulations of Particle Suspensions," Phys. Rev. E, **66**(4), p. 046708.
[52] Dance, S. L., and Maxey, M. R., 2003, "Incorporation of Lubrication Effects into the Force-Coupling Method for Particulate Two-Phase Flow," J. Comput. Phys., **189**(1), pp. 212–238.
[53] Glowinski, R., Pan, T.-W., Hesla, T. I., and Joseph, D. D., 1999, "A Distributed Lagrange Multiplier/Fictitious Domain Method for Particulate Flows," Int. J. Multiphase Flow, **25**(5), pp. 755–794.
[54] Wang, L.-P., Peng, C., Guo, Z., and Yu, Z., 2015, "Lattice Boltzmann Simulation of Particle-Laden Turbulent Channel Flow," Comput. Fluids (in press).
[55] Wu, T., Shao, X., and Yu, Z., 2011, "Fully Resolved Numerical Simulation of Turbulent Pipe Flows Laden With Large Neutrally-Buoyant Particles," J. Hydrodyn. Ser. B, **23**(1), pp. 21–25.
[56] Yu, Z., Wu, T., Shao, X., and Lin, J., 2013, "Numerical Studies of the Effects of Large Neutrally Buoyant Particles on the Flow Instability and Transition to Turbulence in Pipe Flow," Phys. Fluids, **25**(4), p. 043305.
[57] Kim, J., Moin, P., and Moser, R., 1987, "Turbulence Statistics in Fully-Developed Channel Flow at Low Reynolds-Number," J. Fluid Mech., **177**, pp. 133–166.
[58] Moser, R., Kim, J., and Mansour, N. N., 1999, "Direct Numerical Simulation of Turbulent Channel Flow up to Re-Tau = 590," Phys. Fluids., **11**(4), pp. 943–945.
[59] Picano, F., Breugem, W. P., and Brandt, L., 2015, "Turbulent Channel Flow of Dense Suspensions of Neutrally Buoyant Spheres," J. Fluid Mech., **764**, pp. 463–487.
[60] Li, Y. M., McLaughlin, J. B., Kontomaris, K., and Portela, L., 2001, "Numerical Simulation of Particle-Laden Turbulent Channel Flow," Phys. Fluids, **13**(10), pp. 2957–2967.
[61] Segré, G., and Silberberg, A., 1961, "Radial Particle Displacements in Poiseuille Flow of Suspensions," Nature, **189**(476), pp. 209–210.
[62] Segré, G., and Silberberg, A., 1962, "Behavior of Macroscopic Rigid Spheres in Poiseuille Flow," J. Fluid Mech., **14**(1), pp. 136–157.
[63] Shao, X., Yu, Z., and Sun, B., 2008, "Inertial Migration of Spherical Particles in Circular Poiseuille Flow at Moderately High Reynolds Numbers," Phys. Fluids, **20**(10), p. 103307.